Jupiter's Great Red Spot as a Shallow Water System*

Timothy E. Dowling** and Andrew P. Ingersoll

Division of Geological and Planetary Sciences, California Institute of Technology, Pasadena, California

(Manuscript received 18 October 1988, in final form 5 April 1989)

ABSTRACT

Most current models of Jupiter's Great Red Spot (GRS) are cast in terms of a two-layer model, where a thin upper weather layer, which contains the vortex, overlies a much deeper layer, which is meant to represent the neutrally stratified deep atmosphere. Any motions in the deep layer are assumed to be zonal and steady. This two-layer model is dynamically equivalent to a one-layer model with meridionally varying solid bottom topography, called the reduced-gravity model. Specifying the motions, or lack thereof, in the lower layer of the two-layer model is equivalent to specifying the bottom topography, and hence the far-field potential vorticity, in the reduced-gravity model. Current models of the GRS start by guessing the deep motions and then proceed to study vortices using the implied bottom topography. Here, using the GRS cloud-top velocity data, we *derive* the bottom topography, up to a constant that depends on the unknown radius of deformation (or equivalently, the product of the reduced gravity and the mean thickness of the upper layer). The bottom topography is inferred from three quantities derived from the velocity data—Bernoulli streamfunction, kinetic energy per unit mass, and absolute vorticity—all of which are functions only of horizontal position in the reference frame of the vortex. Far from the vortex, potential vorticity versus latitude is calculated from the observed cloud-top zonal velocity and the derived bottom topography. The results show that the deep atmosphere is in differential motion and that the far-field potential vorticity gradient changes sign at several latitudes. Numerical shallow water experiments are performed, using both the derived bottom topography and the bottom topographies prescribed by current models. The results of three published studies are reproduced in our numerical experiments. Each of these models is successful in maintaining a long-lived, isolated vortex, but only the present model yields absolute vorticity profiles along streamlines that agree with those observed for the GRS by Dowling and Ingersoll. In all the models, large vortices form by merging with smaller vortices. In the present, observationally based model, and in one other published model, the smaller vortices arise spontaneously because the observed cloud-top zonal velocity profile is unstable. These two models require an additional momentum source to maintain the upper-layer zonal velocity profile. In the other two models, the bottom topography stabilizes the zonal velocity profile. If dissipation is present, the latter two models require an additional source of smaller vortices to maintain the larger one. A crucial unanswered question for the present model, and for Jupiter itself, is how the cloud-top zonal velocity profile is maintained in its present unstable state.

1. Introduction

The wealth of data returned by the *Voyager* spacecraft encounters of Jupiter in 1979 makes it possible for the first time to study that planet's historically fascinating Great Red Spot (GRS) without specifying a priori the motions in the deep atmosphere. The dynamics of the GRS are coupled to the dynamics of the deep atmosphere, and the cloud-top motions in the GRS and other ovals can be used to probe the underlying fluid motions.

We will consider a two-layer model, where a thin upper weather layer, which contains the vortex, overlies a much deeper layer, which is meant to represent the convectively adjusted, neutrally stratified deep atmosphere. The lower layer is assumed to be much deeper than the upper layer, and is therefore not affected by the upper-layer dynamics (this model is also referred to as the "1½ layer" model). Any motions in the deep layer are assumed to be zonal and steady. This two-layer model is dynamically equivalent to a one-layer model with meridionally varying solid bottom topography, called the reduced-gravity model. Specifying the motions, or lack thereof, in the deep layer of the two-layer model is equivalent to specifying the bottom topography in the reduced-gravity model, and hence the potential vorticity in the far field, that is, far to the east or west of the vortex.

Most current models of the GRS start by making an assumption about the deep motions, and then proceed to study vortices in a reduced-gravity model using the implied bottom topography. Ingersoll and Cuong

(1981) assume that the deep motions are equal to the far-field motions in the upper layer. Williams and Yamagata (1984) and Williams and Wilson (1988) assume that the bottom topography is flat (i.e., solid-body rotation in the deep layer). Marcus (1988) studies a model in which the far-field potential vorticity is constant, and cites evidence that many systems evolve to this state spontaneously. The various bottom topographies prescribed by these models will be discussed in section 3. The work on baroclinic eddies and the GRS by Read and Hide (1983, 1984) is not cast in terms of a one-layer, reduced-gravity model, and will not be directly addressed here.

Instead of guessing the deep motions, in this work we *derive* the bottom topography, up to a constant that depends on the unknown radius of deformation. We use the *Voyager* cloud-top wind data for the GRS and White Oval BC, and make the same reduced-gravity model assumptions as in the models above. Our method of inverting the cloud-top wind data to get the bottom topography is described in section 3. The present approach differs from that of Dowling and Ingersoll (1988), who used the quasi-geostrophic approximation to infer the deep zonal velocity profile. The shallow water (SW) equations used here are more general, and include the quasi-geostrophic approximation as a special case. By assuming that the deep winds are steady and zonal, we make the simplest possible assumption that fits the cloud-top wind data. This assumption includes solid-body rotation of the deep layer as a special case. Our long-range goal is to apply the *Voyager* data to multilayer models like that of Read and Hide. In these cases it may be more difficult to infer the zonal velocity, or the corresponding bottom topography, of the deepest layers.

Once we have deduced the bottom topography for the reduced-gravity SW model of the GRS, we study the system numerically. Our SW numerical scheme is outlined in section 4. We will refer to the derived bottom topography by the label DI89, and the prescribed bottom topographies of Ingersoll and Cuong, Williams and Yamagata, and Marcus by the labels IC81, WY84, and M88, respectively. (The Williams and Wilson bottom topography is equivalent to WY84.) We initialize our runs with the observed zonally averaged cloud-top velocity profile as determined by Limaye (1986). The numerical code is set in oblate spherical geometry. In section 5 we present three types of numerical experiments: (i) model comparisons, (ii) longevity, and (iii) genesis of an isolated vortex. To compare models we make parallel runs, starting with an initial vortex, which differ only in bottom topography. The same Lagrangian vorticity analysis performed on the GRS data (Dowling and Ingersoll 1988) is performed on the model vortices, and the resulting absolute vorticity $(\zeta + f)$ profiles are compared with those for the GRS. Only the DI89 bottom topography yields $(\zeta + f)$ profiles that agree with observations. In many experiments we force the zonal

flow towards the observed cloud-top wind profile on a time scale of 400 days. In the longevity experiment we run a DI89 vortex at full resolution for over ten years. In the genesis experiment we add a small sinusoidal perturbation to the system initialized with the observed zonally averaged cloud-top wind profile and DI89 bottom topography. Several small vortices emerge and then coalesce, until a single large vortex remains and persists.

In section 6 we state our conclusions and point to future work. One important result from this work is a determination of the deep zonal wind profile underneath Jupiter's GRS and White Oval BC, up to essentially a multiplicative constant that depends on the unknown radius of deformation. Another important result is that the observed zonal wind profile is unstable. How the cloud-top winds on Jupiter are maintained in an unstable state is a crucial unanswered question.

No model, including the present one, portrays Jupiter at the level of detail revealed in the *Voyager* images. Figure 1 shows a visual image of Jupiter's cloud tops constructed from *Voyager 1* photographs. The GRS is the largest vortex, centered at about longitude $\phi = 72°$, latitude $\lambda = -22°$. An even larger permanent feature is the turbulent patch directly to the northwest of the GRS, an example of a so-called filamentary region (Ingersoll et al. 1979; Mac Low and Ingersoll 1986). The lifetime of individual features within this region is short—a few days to a week. No model of the GRS to date shows a filamentary region. To successfully model such a feature we expect that the deep motions must be accurately represented. Convective activity, which is beyond the capabilities of the SW model studied here, also appears to play a role in the filamentary regions. Another important observation associated with the GRS is the perpetual existence of several small eddies in the same shear flow as the GRS. Over one dozen small eddies can be seen in Fig. 1 at about latitude $\lambda = -22°$. These eddies are often seen to merge with the GRS. We will return to this point when studying the time evolution of numerical models of the GRS's shear flow in the case where the flow is unstable. Also seen in Fig. 1 are the three White Ovals at about latitude $\lambda = -33°$, and the many other intriguing features of Jupiter's cloud tops. For a complete discussion of the cloud features in Fig. 1 see Smith et al. (1979a,b).

We treat the GRS as a shallow feature. *Voyager* infrared observations have yielded temperature fields above the 500 mb level of the cloud tops, which through application of the thermal wind equation imply a decay of wind strength with height above the clouds (Flasar et al. 1981). The thickness of the GRS from the cloud tops upward is on the order of 100 km. The thickness of the GRS below the cloud tops is a major unknown. We assume that it does not penetrate significantly into the neutrally stratified deep atmosphere, which begins on the order of 100 km below the cloud tops. For a discussion of the deep interiors of Jovian planets see
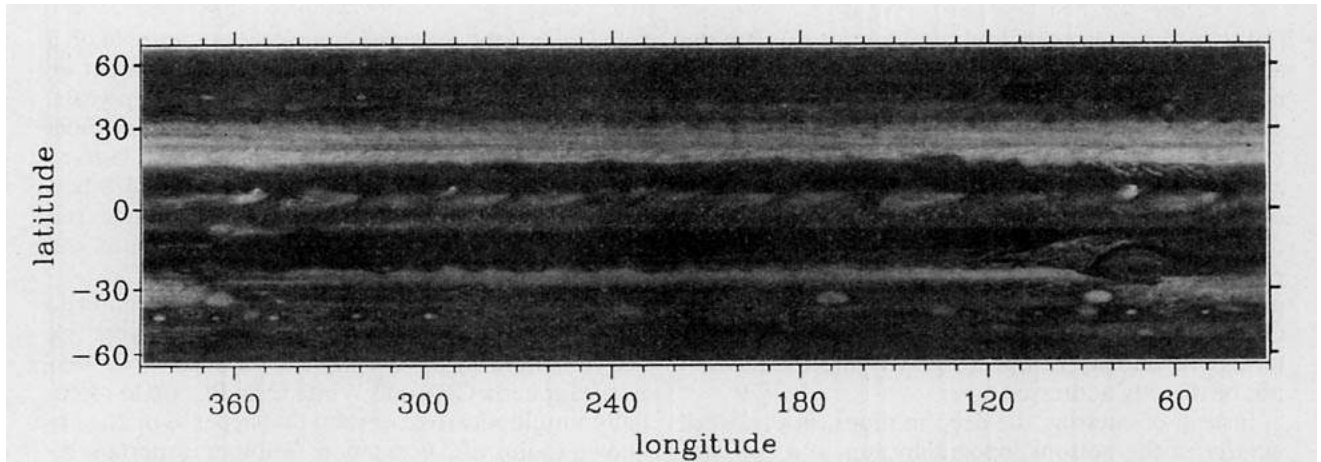
FIG. 1. Visual image of Jupiter's cloud tops. This is a cylindrical mosaic made from *Voyager 1* images, labeled by planetographic latitude and System III (magnetically defined) longitude. Note that longitude increases westward in *Voyager* images and data, but increases eastward in equations and numerical models. The Great Red Spot (GRS) is the large vortex centered at longitude $\phi = 72°$, latitude $\lambda = -22°$. The GRS's filamentary region is the large turbulent patch directly to the northwest of the GRS. Notice that there are over one dozen smaller vortices in the same shear flow as the GRS. The three White Ovals are centered at longitudes $\phi = 5°, 85°$, and $170°$, and latitude $\lambda = -33°$. For a complete description of Jupiter's cloud features see Smith et al. (1979a,b).

Stevenson (1982). Since the GRS covers 20 000 km in longitude, we therefore expect about at 100-to-1 ratio in horizontal to vertical dimensions. For more details see the reviews on Jovian atmospheres by Ingersoll et al. (1984) and Flasar (1986).

2. Shallow water model

We consider a thin upper weather layer (layer 1), supported hydrostatically by a deep layer (layer 2). The density of each layer is assumed to be constant, with the upper-layer density ρ_1 taken to be less than the lower-layer density ρ_2. By specifying constant density layers, we decouple the thermodynamics from the system, while, it is hoped, retaining much of the important dynamics. The upper layer contains the vortices and all the time-dependent motions. The lower layer represents the neutrally stratified deep atmosphere. Since the lower layer is very deep, changes in the height of the layer interface due to upper-layer motions do not significantly change the thickness of the lower layer, and hence have a negligible effect on the deep motions. Any motions in the lower layer are assumed to be zonal and steady. This two-layer system can be reduced to a one-layer system with meridionally varying solid bottom topography (Gill 1982).

The Ingersoll and Cuong (1981) and Marcus (1988) studies used the quasi-geostrophic (QG) equations, while the Williams and Yamagata (1984) and Williams and Wilson (1988) studies used the SW equations. Dowling and Ingersoll (1988) observed that layer thickness and the Coriolis parameter both vary substantially across the GRS, and estimated that the QG approximation is good only to about the nearest 30%. The next step, then, is to use a primitive equation model—the simplest example being the SW equations.

Thus, we will model the GRS as a reduced-gravity SW system, for which the momentum and continuity equations are

$$\frac{\partial u}{\partial t} - (\zeta + f)v = -\frac{1}{r}\frac{\partial}{\partial \phi}[g(h + h_2) + K], \quad (1)$$

$$\frac{\partial v}{\partial t} + (\zeta + f)u = -\frac{1}{R}\frac{\partial}{\partial \lambda}[g(h + h_2) + K], \quad (2)$$

$$\frac{\partial h}{\partial t} + \nabla \cdot (h\mathbf{v}) = 0. \quad (3)$$

The dependent variables u, v, and h are the upper-layer eastward and northward horizontal velocities [$\mathbf{v} \equiv (u, v)$], and the thickness of the upper layer, respectively. The independent variables t, ϕ, and λ are the time, longitude (positive eastward), and planetographic latitude, respectively. We use oblate spherical geometry with radii of curvature r for the zonal direction and R for the meridional direction. If we define the equatorial and polar radii of the planet to be R_e and R_p and set $\epsilon \equiv R_e/R_p$, then

$$r(\lambda) = \frac{R_e}{(1 + \epsilon^{-2}\tan^2\lambda)^{1/2}}, \quad (4)$$

$$R(\lambda) = \frac{R_e}{\epsilon^2}\left(\frac{r}{R_e \cos\lambda}\right)^3. \quad (5)$$

For Jupiter $R_e = 71\ 400$ km and $R_p = 66\ 773$ km. Given a steady state zonal profile for the deep layer, $u_2(\lambda)$, the bottom topography in the reduced-gravity model, $h_2(\lambda)$, is defined by

$$\frac{1}{R}\frac{\partial}{\partial \lambda}gh_2 = -\left(f + \frac{u_2}{r}\sin\lambda\right)u_2. \quad (6)$$

The term $(u_2/r)\sin\lambda$ in (6) is due to the spherical geometry, and is of order 100 times smaller than f. Note that the slope of the bottom topography will change with a change in reference frame. The parameter g is the reduced gravity:

$$g = g_J\left(\frac{\rho_2 - \rho_1}{\rho_2}\right), \qquad (7)$$

where g_J is the actual gravity at Jupiter's cloud tops, which may be assumed constant in our shallow layer. The vertical component of absolute vorticity $(\zeta + f)$ is composed of the relative vorticity $\zeta \equiv \mathbf{k}\cdot(\nabla \times \mathbf{v})$, and the Coriolis parameter $f \equiv 2\Omega\sin\lambda$, where Ω is the planet's angular speed of rotation $(2\pi/\Omega = 9^h 55^m 29.7^s)$. The kinetic energy per unit mass, $\frac{1}{2}(u^2 + v^2)$, is denoted by K.

For many of our numerical experiments we include a forcing/drag term on the right-hand side of (1):

$$-\frac{1}{\tau}(u - u_J(\lambda)) \qquad (8)$$

where τ is typically 400 days, and $u_J(\lambda)$ is the observed zonally averaged cloud-top velocity profile (Limaye 1986). This forcing term, similarly used in Williams and Yamagata (1984), represents a crude attempt at modeling the processes that maintain the observed profile. The value $\tau = 400$ days forces the eastward wind u on a time scale that is much longer than the time scales for dynamical processes such as gravity wave propagation, geostrophic adjustment, merging of vortices, and vortex circulation. Since we will find that forcing an unstable profile leads naturally to the genesis and maintenance of large isolated vortices, understanding the possible physical processes modeled by this simplistic forcing term becomes an important goal for future work.

The form of the pressure-gradient terms in (1) and (2) follows exactly from the equations of hydrostatic balance with zero pressure at the upper free-surface and balanced zonal wind in the deep lower layer. The same equations describe SW motion of a single layer with variable thickness h, solid bottom topography of height h_2, and a gravity field of strength g. However, g is not the gravitational acceleration of Jupiter, and h_2 is not the height of the interface between layers 1 and 2. Equation (7) defines g as the reduced gravity, and (6) defines $\rho_2 g h_2$ as the horizontally varying part of the pressure in the deep layer. The height of the true fluid-layer interface responds to upper-layer motions and varies with latitude, longitude, and time. The bottom topography h_2 in the reduced-gravity system varies only with latitude, if the deep-layer motions are zonal and steady. In the geostrophic limit, the velocity difference between layers 1 and 2 is proportional to the horizontal gradient of the layer thickness h, which follows from (1), (2), and (6).

Equations (1)–(3) conserve such quantities as mass, energy, and enstrophy as global integrals, and they conserve potential vorticity on fluid parcels. Such conservative behavior is clearly an oversimplification. For instance, the weather layer could lose energy by wave radiation into the layers above and below. Achterberg and Ingersoll (1989) have studied this effect in the context of a continuously stratified, quasi-geostrophic system. They find that Jupiter's atmosphere behaves nearly as if it had a rigid lid at a pressure of about 0.7 bars. The sharp increase in static stability at this altitude causes the layers above to reflect energy downward with a reflection coefficient of 0.9 or greater. The transition to the neutrally stable interior occurs at around 5 bars. A normal-mode expansion of motions in the layer 0.7 $\leq P \leq 5$ bars can be truncated to yield a one-layer quasi-geostrophic system analogous to the present SW system.

Flierl (1984) has studied Rossby wave radiation from a thin upper layer into a deeper lower layer. He finds that the rate of energy loss, $(1/E)\partial E/\partial t$, is equal to βL (β is df/dy, L is the horizontal length scale), times a number of order 0.01 (his Fig. 5, lower part), times the ratio of upper-layer thickness to lower-layer thickness. For Jupiter, the latter ratio is essentially zero, so the energy loss should be negligible. Flierl's analysis does not include zonal velocities in the deep layer. As with the Earth's oceans, the interaction between the surface layers and the deep fluid underneath in Jupiter's atmosphere is an important subject that deserves further study.

In a SW system, the horizontal velocities u and v are constant with height in each layer. It is not clear a priori what amplitude of u and v to take for our upper layer that will best represent the real troposphere of Jupiter above and below the cloud tops. The appropriate u and v for the model layer are some type of vertical average over the velocities in the real atmosphere. Achterberg and Ingersoll (1989) find that the appropriate velocity magnitudes for a single weather layer are within 5% of the real cloud-top magnitudes. This finding contrasts with an earlier suggestion by Allison and Gierasch (1982) that the appropriate velocity magnitudes in the model layer are a factor of 2.7 less than the observed cloud-top values. Lowering the velocities in the model would reduce the tendency towards instability. However, we will find that a system in which the winds are strong and unstable naturally produces and maintains large, isolated vortices. Moreover, the observed cloud-top wind profile is in hand, and represents a definite layer of the atmosphere. We will therefore use the observed cloud-top winds to initialize our upper layer. An equally ambiguous problem is how to interpret the deep-layer velocity profiles u_2 that are produced by our analysis in section 3. Our view is that gh_2 and the corresponding u_2 are important parameters of the SW system, and we will infer them from the *Voyager* data.

In our analysis, the reduced gravity g appears only in combination with the variables h and h_2, such as the terms $g(h + h_2)$ or gh_2. We therefore do not have to know or specify the value of $(\rho_2 - \rho_1)/\rho_2$ in (7), which is one advantage of the reduced-gravity notation. We will refer to $g(h + h_2)$ as the free-surface height, and to gh_2 as the bottom topography. Acterberg and Ingersoll (1989) show that for plausible models of the static stability on Jupiter, the values of gh in the reduced-gravity model are of order 1.5×10^4 m^2 s^{-2}. This value assumes solar composition; it is proportional to the assumed water abundance, which is uncertain by at least a factor of 2.

A dynamical variable of central importance is the potential vorticity q, defined by

$$q \equiv \frac{(\zeta + f)}{gh}. \qquad (9)$$

The units of q are s m^{-2}, with our definition differing from the usual one by the inclusion of the constant factor g. In the absence of dissipation, potential vorticity is a conserved quantity following the motion (Gill 1982; Pedlosky 1987):

$$\left(\frac{\partial}{\partial t} + \mathbf{v} \cdot \nabla\right) q = 0. \qquad (10)$$

Dowling and Ingersoll (1988) used this fact to determine layer thickness variations for the GRS and White Oval BC by following $(\zeta + f)$ along streamlines.

In a reference frame that drifts with the GRS, the motions in and near the vortex are observed to be approximately steady. In the steady case there is another conserved variable, the Bernoulli function $B \equiv [g(h + h_2) + K]$. For $\partial/\partial t = 0$, (1) and (2) may be written

$$(\zeta + f)\mathbf{k} \times \mathbf{v} = -\nabla B. \qquad (11)$$

The conservation of B is readily shown by taking the dot product of (11) with $\mathbf{v}$.

The Bernoulli function takes on special significance because it may be computed from the velocity field, via (11). We have calculated B for the GRS and Oval BC, with the results shown as the solid contours in Fig. 2. We use the same velocity data as in Dowling and Ingersoll (1988), which is derived by tracking clouds in *Voyager* images. To begin, we determine u, v, and ζ on a longitude–latitude grid with spacings $\Delta\phi$, $\Delta\lambda$ = 0.5°. These velocity and vorticity fields are calculated, as described in Dowling and Ingersoll (1988), by least-squares fitting to the velocity data inside a local averaging box, where here the averaging box is 3° on a side for both the GRS and White Oval BC. We use the following relaxation technique to compute B. Equation (11) is integrated to find B at the grid point (ϕ, λ) from B at each of the four neighboring points $(\phi + \Delta\phi, \lambda)$, $(\phi - \Delta\phi, \lambda)$, $(\phi, \lambda + \Delta\lambda)$, and $(\phi, \lambda - \Delta\lambda)$. These four values of B are averaged and the result is assigned to (ϕ, λ). To facilitate the calculation,
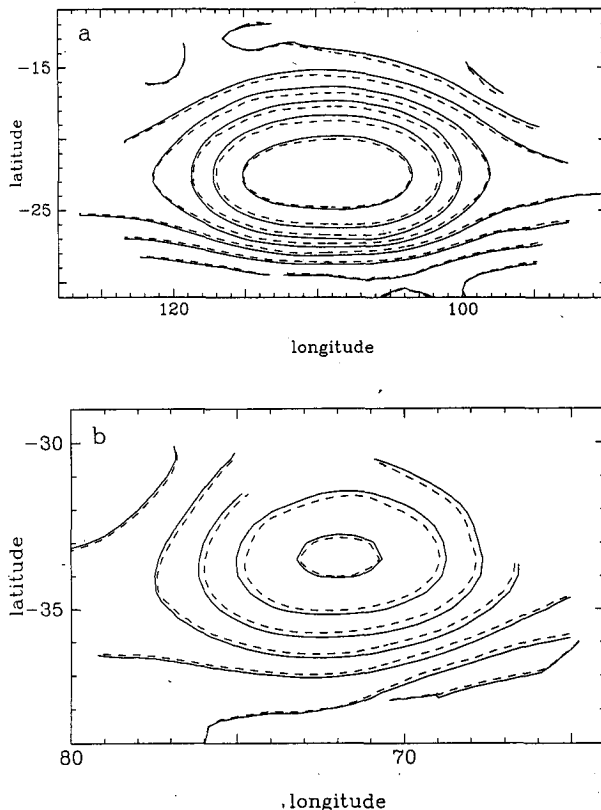

FIG. 2. Bernoulli function B and free-surface height $g(h + h_2)$. (a) The solid and dashed contours show B and $g(h + h_2)$, respectively, for the GRS. These are in the vortex reference frame, with the zero of longitude corresponding to System III on 5 July 1979. The contour interval is 2×10^4 m^2 s^{-2}, with the innermost (highest) closed contour equal to 16×10^4 m^2 s^{-2}. (b) Same as (a) but for the Oval BC. The innermost closed contour is 14×10^4 m^2 s^{-2}.

the $(\zeta + f)u$ and $(\zeta + f)v$ fields are computed on grids staggered by half a spacing from the B grid. For grid points without four neighbors we average over the contributions of the available neighbors. The procedure is iterated until it converges, and produces very satisfactory results. Since B is conserved following the motion, contours of B are streamlines, and those in Fig. 2 compare favorably with the streamlines calculated by direct integration of the (u, v) data (cf. Fig. 2 with Fig. 13). Also plotted as dashed contours in Fig. 2 is the free-surface height $g(h + h_2) = B - K$. Notice that the effect of subtracting K is not large.

Now that we have the B and $g(h + h_2)$ fields for the GRS and Oval BC, we may proceed to determine gh_2 for these vortices. Section 3 contains our method for inverting the velocity data to obtain gh_2, as well as the resulting deep winds and far-field potential vorticities, for the GRS and Oval BC.

3. Calculation of bottom topography

Using (9) and the definition of B, the bottom topography gh_2 may be expressed as:

$$gh_2 = (B - K) - \frac{1}{q}(\zeta + f). \qquad (12)$$

Since B, K, and $(\zeta + f)$ are observable, the only unknown on the right-hand side of (12) is q. On a streamline both q and B are constant, so we may label streamlines with B and write $q = q(B)$, taking care to allow $q(B)$ to be multivalued when different streamlines have the same B value.

We model the function $1/q(B)$ as piecewise quadratic:

$$1/q(B) = 1/q_0 + (1/q_1)_j b + (1/q_2)_j b^2,$$

$$b \equiv (B/B_0 - 1), \qquad (13)$$

where B_0 marks the largest closed streamline, and the subscript j refers to each region in which $q(B)$ is assumed to be quadratic. For the GRS (Fig 2a) $B_0 = 8.3 \times 10^4$ m^2 s^{-2}. We label as N and S the northern and southern open streamline regions, defined by $B \le B_0$ and λ greater or less than $-23°$, respectively. The critical open streamline that divides the N and S open streamline regions occurs at the latitude $\lambda_0 = -23°$ for the GRS and at $\lambda_0 = -34.5°$ for the Oval BC. These critical streamlines are important because they allow us to connect to the far field in a consistent manner. We find it convenient to divide the closed streamline region, $B > B_0$, into two regions labeled C for "central" and I for "inner." For the GRS the region C is defined by $15.6 \ge B > 8.3 \times 10^4$ m^2 s^{-2}, and the region I is defined by $B > 15.6 \times 10^4$ m^2 s^{-2}. This subdivision allows better handling of the crossover into the quiescent inner region of the GRS, which is large in area but corresponds to a small interval of B. For the Oval BC, $B_0 = 7.1$ m^2 s^{-2}; N and S are defined by $B \le B_0$ and λ greater or less than $-34.5°$, respectively; C is defined by $13.1 \ge B > 7.1 \times 10^4$ m^2 s^{-2}, and I is defined by $B > 13.1 \times 10^4$ m^2 s^{-2}.

The form of (13) is such that $1/q(B_0) = 1/q_0$. We treat $1/q_0$ or q_0 for the GRS as our one free parameter, and invert the data to obtain the $(1/q_1)_j$ and $(1/q_2)_j$ in (13). Although we do not use the quasi-geostrophic approximation in this paper, we can relate q_0 to an effective radius of deformation for the system, L_d. If H denotes a characteristic depth of the upper layer, and f_0 a characteristic Coriolis parameter, then

$$L_d \equiv \frac{(gH)^{1/2}}{|f_0|}. \qquad (14)$$

The Rossby numbers for the GRS and Oval BC are not greater than 0.36 (Mitchell et al. 1981) so that $|\zeta| < f_0$ and hence $q_0 \sim f_0/(gH)$. Thus,

$$L_d \sim \frac{1}{(f_0 q_0)^{1/2}}. \qquad (15)$$

We will use (15) to relate the parameter q_0 to the more familiar parameter L_d.

The bottom topography under each vortex is modeled as a quartic in latitude, i.e.,

$$gh_2 = A_0 + A_1\lambda + A_2\lambda^2 + A_3\lambda^3 + A_4\lambda^4. \qquad (16)$$

The data require at least a quadratic profile for the bottom topography, as shown in Dowling and Ingersoll (1988). The quartic gh_2 model allows a cubiclike profile for $u_2(\lambda)$, which is appropriate if the deep winds consist of alternating east–west jets.

We now substitute (13) and (16) into (12) to get

$$B - K - \frac{1}{q_0}(\zeta + f) = A_0 + A_1\lambda + A_2\lambda^2 + A_3\lambda^3$$
$$+ A_4\lambda^4 + [(1/q_1)_j b + (1/q_2)_j b^2](\zeta + f), \qquad (17)$$

where the left-hand side is the input data and the right-hand side is the model. The input data are arranged on the longitude–latitude grid used to calculate B in section 2. Equation (17) is linear in the 13 unknown A and $1/q$ coefficients, and we solve it by the method of least squares. Once the value of q_0 is specified for the GRS, a corresponding value for the Oval BC is fixed, as described below. In Table 1 we list results for the coefficients in (13) and (16), for three such paired values of q_0 for the GRS and Oval BC. Note that the A coefficients apply in the reference frame of each vortex. To change reference frames, replace u_2 defined in the vortex frame with u_2 defined in the System III (magnetically defined) frame, and use (6) to adjust gh_2 accordingly. The drift rates for the GRS and Oval BC relative to the System III reference frame were calculated in Dowling and Ingersoll (1988) to be -0.258 ± 0.001 deg day^{-1} (westward drift) and 0.392 ± 0.007 deg day^{-1} (eastward drift), respectively.

Figure 3 shows q versus B for the case $q_0 = -1.40 \times 10^{-9}$ s m^{-2} for the GRS. This value of q_0 translates via (15) into an L_d of 2300 km (for $f_0 = -1.35 \times 10^{-4}$ s^{-1}). The difference in the N and S curves for the GRS (Fig. 3a), as opposed to the lack of difference in those curves for the Oval BC (Fig. 3b), probably stems from the fact that B is noticeably steeper on the southern side of the GRS than the northern side. For other values of q_0, the solutions for $q(B)$ resemble those shown in Fig. 3, but shifted up or down the ordinate.

We tested the sensitivity of our results to the piecewise quadratic model for $q(B)$ by trying various alternatives, including piecewise linear through piecewise quartic functions, and by trying the regions C and I combined and separate. The resulting $q(B)$ depend very little on our model choice. For instance, combining regions C and I and assuming a quartic model for $q(B)$ in this combined region yields virtually the same profile as in Fig. 3, including the kink that marks the boundary between C and I. One measure of error is the spread in the results from all these approaches, which we will indicate when we compare GRS models.

Figure 4 shows the derived gh_2 and u_2 in the System III reference frame. The solid curves in Fig. 4a show

TABLE 1. Results for model coefficients in (13) and (16). *Note:* λ in radians, B_0(GRS) = 8.3×10^4 m^2 s^{-2}, B_0(BC) = 7.1×10^4 m^2 s^{-2}; gh_2 in vortex reference frame, in units of 10^4 m^2 s^{-2}; q in units of 10^{-9} s m^{-2}.

	GRS	BC	GRS	BC	GRS	BC
q_0	−2.30	−3.70	−1.40	−1.84	−1.00	−1.21
$(1/q_1)_N$	−1.146	−0.525	−1.264	−0.630	−1.384	−0.740
$(1/q_2)_N$	−0.589	−0.390	−0.626	−0.603	−0.664	−0.824
$(1/q_1)_S$	−0.465	−0.355	−0.536	−0.367	−0.608	−0.380
$(1/q_2)_S$	−0.084	−0.045	−0.182	−0.029	−0.282	−0.012
$(1/q_1)_C$	−0.197	−0.165	−0.096	−0.123	0.007	−0.079
$(1/q_2)_C$	−0.864	−0.544	−1.092	−0.755	−1.325	−0.974
$(1/q_1)_I$	−3.232	−1.119	−3.990	−1.564	−4.765	−2.025
$(1/q_2)_I$	2.552	0.562	3.307	0.934	4.078	1.320
A_0	65.30	5 138.95	80.28	10 352.75	95.60	15 752.84
A_1	775.2	35 527	968.3	71 243	1166	108 235
A_2	3460	91 629	4240	182 901	5036	277 435
A_3	6599	104 560	7956	207 781	9342	314 690
A_4	4477	44 537	5302	88 121	6146	133 261

gh_2 for various values of q_0. The dashed curve is the far-field free-surface height $g(\bar{h} + h_2)$, where the overbar denotes a far-field profile, calculated by integrating (2), using the observed zonal wind profile $u = u_J$, and $v = 0$. The constant of integration is determined by matching q at the latitude λ_0 where the largest closed streamline merges with the critical open streamline. Thus, we require $\bar{q}$ at latitude λ_0 be equal to $q_0 \equiv q(B_0)$. This fixes $g\bar{h}$ to be equal to $(\bar{\zeta} + f)/q_0$ at $\lambda = \lambda_0$. The distance between the dashed and solid curves in Fig. 4a gives $g\bar{h}$ versus latitude in the far field for each choice of q_0. The error bars on the gh_2 curves in Fig. 4a indicate the variation of the data about each model fit, and are two standard deviations in total length. Our procedure for linking the bottom topographies determined from the GRS and Oval BC is as follows. First, we specify q_0 for the GRS, then determine gh_2 in the GRS reference frame, and shift it into the System III reference frame, using (6), thus yielding gh_2 over the latitudes −31° to −11°. The Oval BC data apply over the latitudes −39° to −30°. We vary q_0 for the Oval BC until it gives a gh_2 profile which, in the System III reference frame, matches the gh_2 from the GRS data at latitude $\lambda = -30.5°$. Thus specifying q_0 for the GRS fixes q_0 for the Oval BC, through continuity of gh_2. The gh_2 profiles in Fig. 4a are labeled by q_0 for the GRS, in units of 10^{-9} s m^{-2}. The connection at $\lambda = -30.5°$ is smoothed by fitting a parabola to the points in the interval $-30.5 \pm 2°$. In Fig. 4b we show the u_2 profiles in the System III frame, calculated from (6) using the gh_2 profiles in Fig. 4a. (In this calculation we neglect the $(u_2/r)\sin\lambda$ term in (6), which introduces less than 1% error in the u_2 determination.)

The deep layer results are intriguing. In the context of the SW equations, we are seeing the signature of differential motion in the deep atmosphere. We suspect that the small thickness (small $g\bar{h}$) of the upper layer

in the latitudes northward of −20° (Fig. 4a) is intimately related to the existence of the GRS's filamentary region. Convection, were it possible in a SW system, might correspond to negative upper-layer thickness $g\bar{h}$. Since convective plumes appear to form regularly in the GRS's filamentary region, perhaps the appropriate q_0 is one that actually makes $g\bar{h}$ negative there. Negative gh occurs for $q_0 < -3.2 \times 10^{-9}$ s m^{-2}, which by (15) corresponds to an effective $L_d < 1520$ km (for $f_0 = -1.35 \times 10^{-4}$ s^{-1}). The u_2 profile for this limiting case is nearly the same as that shown in Fig. 4b for the case $q_0 = -2.3 \times 10^{-9}$ s m^{-2}. The biggest differences between the derived u_2 profiles in Fig. 4b and the cloud-top winds occur in the latitude band of the GRS's filamentary region. Our results imply that wind speeds in the cloud-top westward jet at $\lambda \sim -20°$ decay rapidly with depth. In contrast, the u_2 profiles under the Oval BC are fairly similar to the zonally averaged cloud-top winds. Clearly, at this point we could use some additional data to pin down q_0. We tend to favor those values of q_0 ($-3.2 < q_0 \times 10^9 < -1.4$) that yield small values of $g\bar{h}$, as these are more in line with the values calculated by Achterberg and Ingersoll (1989). We will concentrate on the case $q_0 = -1.4 \times 10^{-9}$ s m^{-2} ($L_d \sim 2300$ km) in the remainder of this paper, since we have not found any significant qualitative differences between it and the extreme cases.

Once we have gh_2, we may determine the far-field potential vorticity of the system, using (9). The Limaye profile of zonal velocity is used to compute the far-field $\bar{\zeta}$ and $g(\bar{h} + h_2)$ profiles, and hence the far-field $\bar{q}$ profile. In Fig. 5 the dashed curve shows $\bar{q}$ versus latitude for the case $q_0 = -1.40 \times 10^{-9}$ s m^{-2} for the GRS. The error bar indicates the variation of the data about the model fit, and is two standard deviations in total length. Instability of the zonal flow is possible where $\bar{q}$ has a local extremum. For a recent analysis of
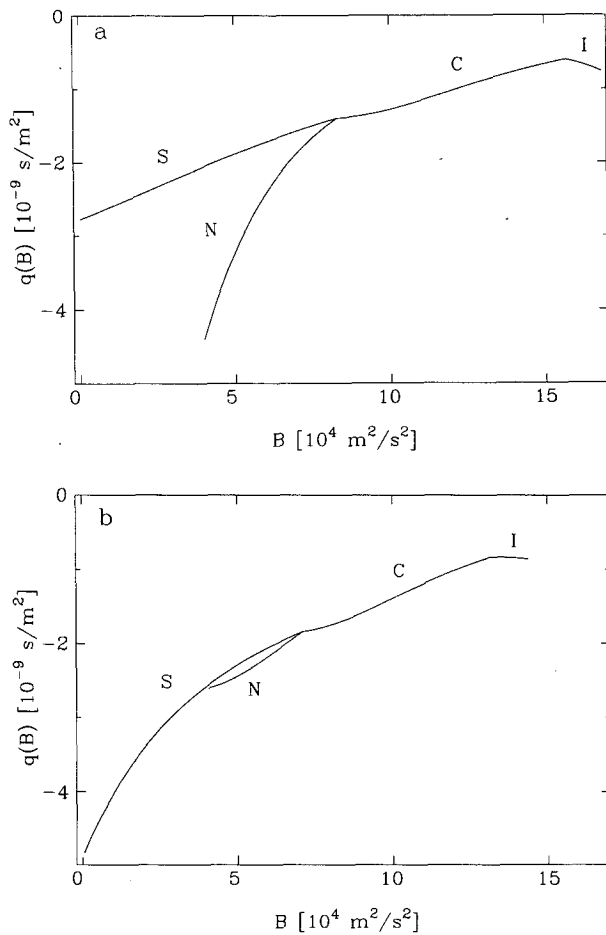
FIG. 3. Potential vorticity q versus Bernoulli function B. (a) Model results for the GRS. Different functions $q(B)$ are allowed for the northern and southern open streamline regions, denoted by N and S, respectively. The central closed streamline region is split into two pieces, denoted by C and I. The inner region I is defined by $B > 15.6 \times 10^4$ m^2 s^{-2}, the region C is defined by $15.6 \geqslant B > 8.3 \times 10^4$ m^2 s^{-2}, and the regions N and S are defined by $B \leqslant 8.3 \times 10^4$ m^2 s^{-2}, with latitude greater or less than $-23°$, respectively. Refer to Fig. 2a for a map of B. The function $1/q(B)$ is assumed to be piecewise quadratic in each region. The constant term $1/q_0$ is specified and equals $1/(-1.40 \times 10^{-9}$ s m$^{-2})$ in this figure. (b) Same as (a) but for the Oval BC. The region I is defined by $B > 13.1 \times 10^4$ m^2 s^{-2}, the region C is defined by $13.1 \geqslant B > 7.1 \times 10^4$ m^2 s^{-2}, and the regions N and S are defined by $B \leqslant 7.1 \times 10^4$ m^2 s^{-2}, with latitude greater or less than $-34.5°$, respectively. The specified parameter $1/q_0$ equals $1/(-1.84 \times 10^{-9}$ s m$^{-2})$.

the stability of zonal flows in a SW system see Ripa (1983). We will examine the stability of this system numerically in section 5. Marcus (1988) argues that the far-field potential vorticity should be uniform. Our results in Fig. 5 imply a nonuniform distribution. The disagreement will show up clearly in the Lagrangian ($\zeta + f$) analysis of an M88 vortex, discussed in section 5. In Fig. 5 the solid curves are profiles of q versus latitude through the centers of the GRS and Oval BC. These are computed using the calculated functions

$B(\phi, \lambda)$ and $q(B)$ shown in Figs. 2 and 3, respectively. It is interesting to note that the GRS and Oval BC appear as minimum $|q|$ anomalies, that q in the inner regions of these vortices is relatively uniform, and that the drop-off of q to the far-field profile is fairly symmetric on the northern and southern ends of the vortices. Rhines and Young (1982) discuss the homogenization of potential vorticity in the interior of closed-streamline regions. Marcus (1988), using the velocity profiles of Mitchell et al. (1981), reached a conclusion similar to ours, namely, that the potential vorticity in
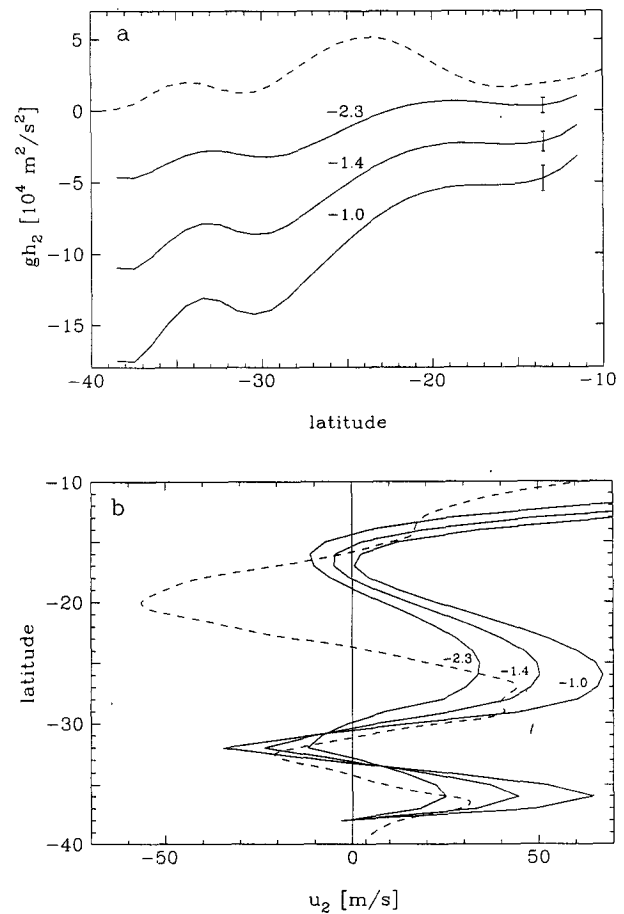

FIG. 4. Bottom topography gh_2 and deep-layer velocity u_2, in the System III reference frame. (a) The dashed curve shows the far-field free-surface height $g(\bar{h} + h_2)$ calculated from the cloud-top zonal wind profile of Limaye (1986). The solid curves show different solutions for the bottom topography gh_2 inferred from the data. See the text for a description of the data inversion method. The error bars indicate the variation of the data about each model fit, and are two standard deviations in total length. The curves are labeled by the parameter q_0 in units of 10^{-9} s m^{-2}. The bottom topographies under the GRS and Oval BC are assumed to be quartics in latitude, and are spliced together by fitting a parabola to the points in the interval $-30.5 \pm 2°$. The results are presented in the System III reference frame, with the zero of the ordinate defined to be the minimum of the curve $g(\bar{h} + h_2)$. (b) The dashed curve shows the cloud-top wind profile of Limaye. The solid curves show different solutions for the deep-layer velocity u_2, corresponding to the gh_2 presented in (a).
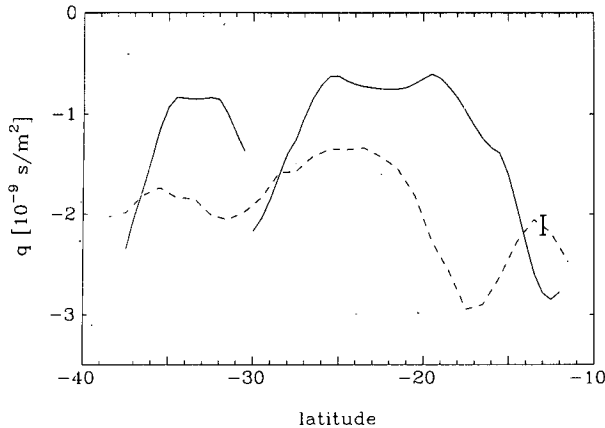
FIG. 5. Potential vorticity q versus latitude λ. The dashed curve shows the far-field potential vorticity $\bar{q}$, calculated from the cloud-top zonal winds and inferred bottom topography (Fig. 4). The case presented has $q_0 = -1.40 \times 10^{-9}$ s m^{-2} for the GRS. The error bar indicates the variation of the data about the model fit, and is two standard deviations in total length. Instability of the flow is possible where $\bar{q}$ is a local extremum. The solid curves show profiles of q versus λ through the centers of the GRS (right curve) and Oval BC (left curve). These are computed using the calculated functions $B(\phi, \lambda)$ and $q(B)$ shown in Figs. 2 and 3, respectively.

the inner regions of the GRS and Oval BC is approximately uniform.

We now turn to a comparison of the derived (DI89) gh_2 and far-field $\bar{q}$ with those prescribed by current models. For the DI89 case, we use $q_0 = -1.40 \times 10^{-9}$ s m^{-2} for the GRS, along with the corresponding $q_0 = -1.84 \times 10^{-9}$ s m^{-2} for the Oval BC. For the other models we take $q_0 = -1.40 \times 10^{-9}$ s m^{-2} at $\lambda = -23°$, which completely determines $gh_2(\lambda)$. The IC81 model prescribes u_2 to be equal to the zonally averaged cloud-top winds, which is the same as setting $g\bar{h} = $ const. $= [(\bar{\zeta} + f)/q_0]_{\lambda=-23°}$. The WY84 model prescribes flat bottom topography, which implies $u_2 = 0$. For this model we take $gh_2 = $ const. $= [g(\bar{h} + h_2) - (\bar{\zeta} + f)/ q_0]_{\lambda=-23°}$. The M88 model prescribes constant far-field $\bar{q}$, which implies $g\bar{h} = (\bar{\zeta} + f)/q_0$.

In Fig. 6a we plot gh_2 for the four models DI89, IC81, WY84, and M88. The solid curve is the DI89 bottom topography, with the error bar on the right indicating the maximum variation of this profile over the entire region for the various models of the function $q(B)$ discussed at the beginning of this section. Notice that while some of the prescribed gh_2 agree with the derived gh_2 over certain ranges of latitude, none of them shows qualitative agreement over the entire latitude range observed. In Fig. 6b we show the corresponding far-field potential vorticity profiles. Both the DI89 and WY84 potential vorticity profiles show significant local extrema, which implies the possibility of instability for these models. We will run numerical models of the GRS in section 5 using the various gh_2 shown in Fig. 6a. In section 4 below we describe our numerical scheme.

4. Numerical scheme

We use the Arakawa and Lamb (1981) potential enstrophy and energy conserving scheme for the SW equations. This finite difference scheme is particularly suited to long-term integrations, especially when bottom topography is present. The Arakawa and Lamb scheme was also used by Williams and Wilson (1988). Because we want to incorporate observed cloud-top wind data, and to perform the same analysis on our simulations as done for the GRS and Oval BC in Dowling and Ingersoll (1988), we use full oblate spherical geometry.
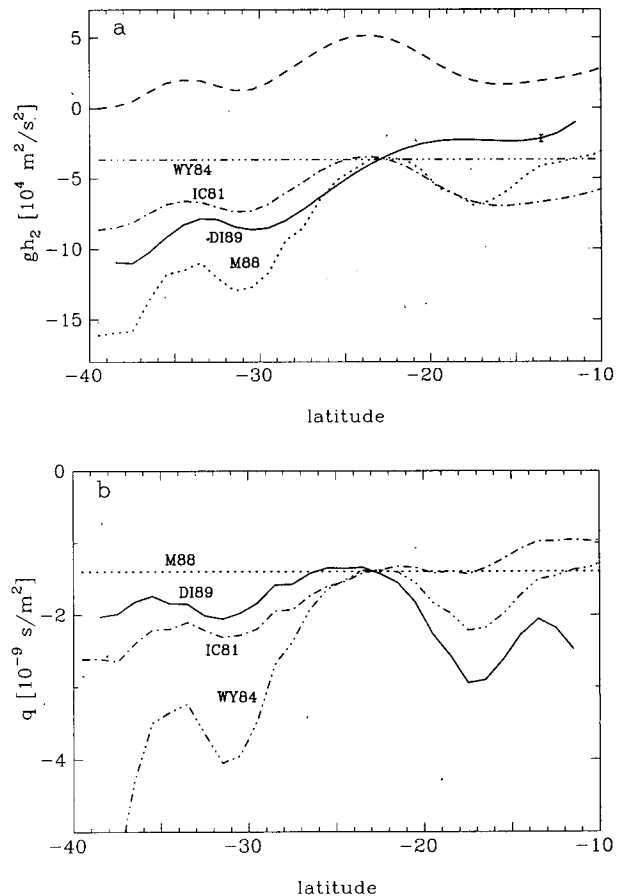

FIG. 6. Bottom topographies gh_2 and far-field potential vorticity $\bar{q}$ for current models of Jovian vortices. (a) The dashed curve shows the far-field free surface height $g(\bar{h} + h_2)$ calculated, in the System III reference frame, from the cloud-top zonal wind profile of Limaye (1986). The solid curve, denoted by DI89, shows the bottom topography inferred from the data (this work) for the case $q_0 = -1.40 \times 10^{-9}$ s m^{-2} for the GRS, with the corresponding $q_0 = -1.84 \times 10^{-9}$ s m^{-2} for the Oval BC. The error bar on the right indicates the maximum variation of this bottom topography solution for various models of the function $q(B)$, as described in the text. The curves denoted by IC81, WY84, and M88 show bottom topographies (in the System III reference frame) prescribed by the Jovian vortex models of Ingersoll and Cuong (1981), Williams and Yamagata (1984), and Marcus (1988), respectively. (b) Corresponding far-field potential vorticities $\bar{q}$ for the models shown in (a).

The simulations are carried out on staggered longitude–latitude grids with 1° spacing. Relative to the grid on which vorticity is defined, u is computed on a grid shifted half a spacing northward, v is computed on a grid shifted half a spacing eastward, and gh is computed on a grid shifted half a spacing northward and half a spacing eastward. Since the GRS is about 20° by 10° in size, a 1° grid spacing is found to be quite adequate in resolving GRS-sized vortices. The domain is taken to be −90° to 90° in longitude and −40° to −5° in latitude. The latitude range is sufficient to contain alternating jets to the north and south of the GRS shear zone, and to isolate the region of study from the boundaries. We use a time step of 15 minutes, which is small enough to prevent numerical instability, and provides adequate temporal resolution. Halving this time step has little effect on the simulations. Both the Williams and Yamagata (1984) and Williams and Wilson (1988) studies used similar domain sizes, and spatial and temporal resolutions.

We use periodic boundary conditions on the eastern and western boundaries. Because of the staggering of the variables, only v and q fall on the northern and southern boundaries, for which we specify $v = 0$, and $q = q_J$. The latter is a computational boundary condition with q_J equal to the potential vorticity calculated from the observed zonally averaged cloud-top wind profile u_J and the particular bottom topography of the model.

The time integration is started with an Euler-backward (Matsuno) time step, followed by 11 leapfrog (centered difference) steps. This sequence is then repeated. The Euler-backward step serves to prevent the odd–even separation of the leapfrog steps, and through its dissipative properties at small scales (Haltiner and Williams 1980), represents the only source of viscosity in the system. With this scheme we did not find it necessary to use explicit dissipative terms or time smoothing to suppress small scale noise and prevent numerical instability. The small loss of total energy to the system from the dissipative Euler-backward time step corresponds to about the loss of the kinetic energy in a 100 m s^{-1} jet every 1000 years.

In many of our experiments we force the u component of velocity by adding the forcing/drag term (8) to the right-hand side of (1), as described in section 2. (Notice that we do not add a term like $-v/\tau$ to (2), which would inhibit meridional motions.) Since this term is parabolic it should not be centered differenced (Haltiner and Williams 1980), and we use forward differencing.

To initialize a run, we specify u, v, and gh at time $t = 0$, and the bottom topography gh_2. The bottom topography is specified by the given model, as discussed in section 3. The free-surface height $g(h + h_2)$ is always initialized geostrophically from u_J, with the result shown as the dashed curve in Fig. 4a. If desired, a disturbance is then added to the $g(h + h_2)$ field, followed by geostrophic initialization of the u and v fields. The gh field is then computed by subtracting gh_2 from $g(h + h_2)$. A run of 250 simulated days (1 day ≡ 24 hours) takes 4 CPU minutes on the San Diego Supercomputer Center's Cray X-MP/48, or 40 CPU hours on our μVax.

In section 5 we use this numerical SW scheme to examine the time evolution of the various models of the GRS described in section 3. We then perform the same Lagrangian vorticity analysis on the model vortices as was done for the GRS and White Oval BC in Dowling and Ingersoll (1988). Next, we use the numerical scheme to examine the longevity and genesis of the present DI89 model of the GRS.

5. Numerical experiments

a. Model comparisons

We now examine the effect of changing the bottom topography on a vortex embedded in the observed cloud-top zonal winds of Jupiter. In Fig. 7 we show the initial free-surface height $g(h + h_2)$ for the model comparison experiments. This initial state is constructed by adding a bump of GRS-like dimensions to the free-surface height calculated from the observed cloud-top wind profile, u_J, of Limaye (1986). Figure 6a shows the geometry prior to adding the initial vortex
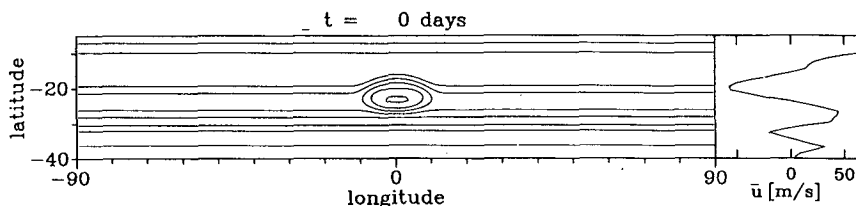
FIG. 7. Initial free-surface height $g(h + h_2)$ for the model comparison experiments. This initial state is constructed by adding a GRS-like vortex, described in the text, to the free-surface height calculated from the cloud-top zonal winds, and by geostrophically initializing the velocity field. The peak wind in the initial vortex is 91 m s^{-1} (System III). The contour interval for plots in this section is 1.5×10^4 m^2 s^{-2}, with the initial minimum $g(h + h_2)$ defined to be the zero contour, occurring at $\lambda = -40°$, and the innermost closed contour here equal to 9×10^4 m^2 s^{-2}. The right panel shows the zonally averaged eastward wind $\bar{u}$ in the System III reference frame.

for each bottom topography to be considered. In the DI89 case, the numerical domain ($-40°$ to $-5°$ in latitude) is slightly larger than the data coverage ($-39°$ to $-11°$ in latitude). We extend the DI89 topography to the ends of the numerical domain by assuming constant gh in the end regions. The particular manner in which this extension is made is found to have little effect on the simulations. The initial vortex bump is given by:

$$a_1 \exp\left(-\left[\frac{(\phi - \phi_0)^2 + a_2(\lambda - \lambda_0)^2}{a_3^2}\right]^2\right), \quad (18)$$

where $a_1 = 4 \times 10^4 \text{ m}^2 \text{ s}^{-2}$, $a_2 = 3$, $a_3 = 9°$, $\phi_0 = 0°$, and $\lambda_0 = -21.5°$. We use a squared Gaussian instead of a Gaussian to imitate more closely the real GRS, which, because of its quiescent central region, has a relatively flat top (Fig. 2a). The parameters in (18) were chosen so that the resulting radial velocity and vorticity profiles resemble those of the GRS (Mitchell et al. 1981).

The first numerical run is for the DI89 bottom topography without the zonal forcing/drag term, i.e., using (1) without the additional term (8). Initially, the westward jet that flows around the northern side of the vortex creates a pattern suggestive of the filamentary region to the northwest of the GRS. This pattern can be seen in the $t = 20$ days time frame in Fig. 8. At this early time the zonal average of the eastward velocity $\bar{u}$, shown in the right panel, is still quite close to the initial profile. However, this is a transitory phase. By $t = 200$ days, $\bar{u}$ has smoothed out noticeably, and small eddies have begun to form in the $g(h + h_2)$ field. This instability of the shear flow is consistent with the existence of extrema in the far-field potential vorticity (Fig. 6b). The big vortex settles into a drift rate of about 0.33 deg day^{-1}, to be compared with the GRS drift rate of -0.258 ± 0.001 deg day^{-1}. The model vortex moves slowly enough so that the apparent drift from frame to frame is the actual drift. The peak wind in the vortex at $t = 1000$ days is 110 m s^{-1}. Notice that it has grown in size by $t = 1000$ days, at the expense of the shear zone. The shape of the vortex at $t = 1000$ days is triangular, with a large penetration into the eastward jet on the southern side of the vortex. This triangular shape does not resemble the GRS, and suggests that the zonal winds on Jupiter are stiffened in some way. That the $\bar{u}$ profile smooths out with time also suggests that we should examine a case in which we force the zonal flow.

In Fig. 9 we show a DI89 run identical to that in Fig. 8 except that now we force the eastward velocity u towards u_J on a time scale $\tau = 400$ days by adding the term (8) to the right-hand side of (1). At $t = 20$ days the vortex is virtually identical to the previous case, again showing structure to the northwest that is suggestive of the GRS's filamentary region. By $t = 200$

days, the effects of the zonal forcing/drag term become noticeable. The vortex throughout this run maintains an excellent GRS-like shape, and settles into a drift rate of about 0.22 deg day^{-1}. We will compute absolute vorticity ($\zeta + f$) profiles along streamlines (i.e., Lagrangian profiles) for this vortex, at $t = 1000$ days, and compare directly with the GRS observations of Dowling and Ingersoll (1988). The $\bar{u}$ profile at $t = 1000$ days resembles the initial profile somewhat better than in the previous case (Fig. 8), but the strength of the westward jet at $\lambda = -20°$ is still reduced by about 10 m s^{-1}, and there is no persistent structure analogous to a filamentary region. Getting a permanent filamentary region is probably going to require a model with higher horizontal and vertical spatial resolution, a more physically correct forcing mechanism, and some simulation of convection, in addition to having the proper deep-atmospheric motions.

In Fig. 10 we show an IC81 run without the forcing/drag term ($\tau = \infty$). This run is the same as in Fig. 8, except for the change to the IC81 bottom topography. Differences between the DI89 and IC81 vortices can already be seen at $t = 20$ days. The IC81 vortices we have examined all drift westward at high speed, with this one moving at about -3.25 deg day^{-1}—over ten times faster than the GRS drift rate. The shear flow does not break up into small eddies, consistent with the lack of significant extrema in the far-field potential vorticity (Fig 6b). As shown by Ingersoll and Cuong (1981), the vortex persists indefinitely for this inviscid case ($\tau = \infty$). Adding the forcing/drag term causes the vortex to decay on a time scale given by τ, in contrast to the DI89 vortex of Fig. 9. There, the vortex maintains itself by merging with smaller vortices that are continuously being produced in the unstable shear flow. Here, the shear flow is stable, and the larger vortex has no smaller vortices on which to feed. We will examine Lagrangian ($\zeta + f$) profiles for the IC81 vortex at $t = 1000$ days.

In Fig. 11 we show a WY84 run ($\tau = 400$ d). This run is the same as in Fig. 9 except for the change to WY84 bottom topography. Again, differences can be seen between the WY84 vortex and the previous models as early as $t = 20$ days. Like the DI89 vortex, the WY84 vortex initially shows interesting structure in the flow around it. The shear flow is quite unstable and we found it necessary to run the model out to $t = 1600$ days before it settled into a quasi-steady state. The vortex drifts at about -1.88 deg day^{-1} in this experiment, but the drift rate tends to depend on the initial placement of the vortex and can be made closer to the GRS drift rate. The $\bar{u}$ profile at $t = 1600$ days is much weaker than the observed initial profile, and the vortex is correspondingly much stronger. Notice that the zonally averaged velocity at the latitude of the White Oval ($\lambda = -33°$) is greatly reduced in magnitude, presumably related to the shallowness and instability of the upper layer in that region for this model.
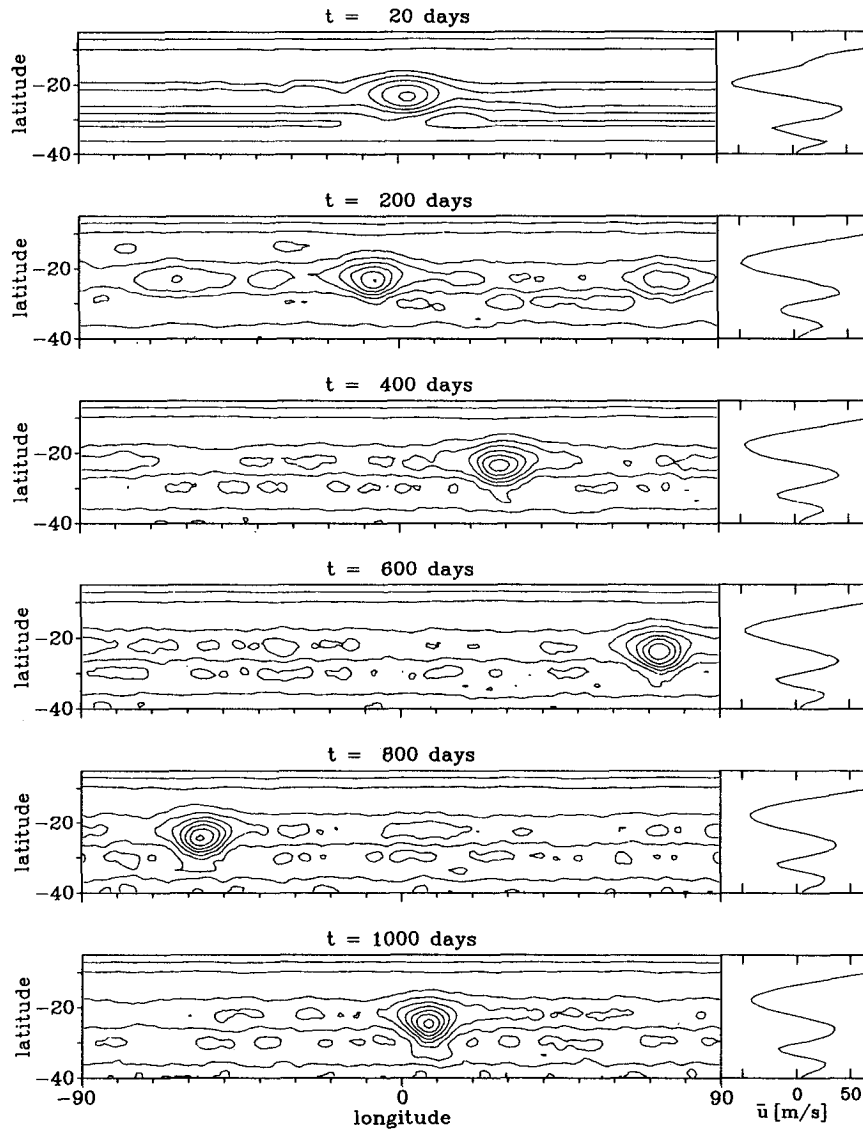
FIG. 8. Free-surface height $g(h + h_2)$ for the DI89 run without zonal forcing ($\tau = \infty$). The initial height field is shown in Fig. 7, and the bottom topography gh_2 is shown in Fig. 6a. The vortex settles into a drift rate of about 0.33 deg day^{-1} in the System III reference frame, to be compared with the GRS drift rate of -0.258 ± 0.001 deg day^{-1} (Dowling and Ingersoll 1988). The model vortex moves slowly enough so that the apparent drift from frame to frame is the actual drift. The peak wind in the vortex at $t = 1000$ days is 110 m s^{-1}.

We will examine Lagrangian ($\zeta + f$) profiles of the WY84 vortex at $t = 1600$ days.

In Fig. 12 we show an M88 run, without the forcing/drag term ($\tau = \infty$). This run is the same as in Figs. 8 and 10 except for the change to M88 bottom topography. Since the far-field potential vorticity is uniform by design, the zonal velocity profile is stable. As in the IC81 case, numerical simulations confirm that the initial zonal velocity profile and the vortex persist indefinitely. If the forcing/drag term (8) is added, the vortex decays on a time scale given by τ. Thus, both the IC81 and M88 models require something external to the

present system to maintain their vortices against dissipation, while both the DI89 and WY84 models require forcing to maintain their zonal velocity profiles against instability. We will examine Lagrangian ($\zeta + f$) profiles for the M88 vortex at $t = 1000$ days.

The Lagrangian vorticity results for the GRS from Dowling and Ingersoll (1988) are reproduced in Fig. 13. The top panel shows the selected GRS streamlines used in the analysis, labeled a–h. The bottom panels show absolute vorticity ($\zeta + f$) profiles, along streamlines, versus latitude λ. These profiles are proportional to the layer thickness gh, since q is constant along
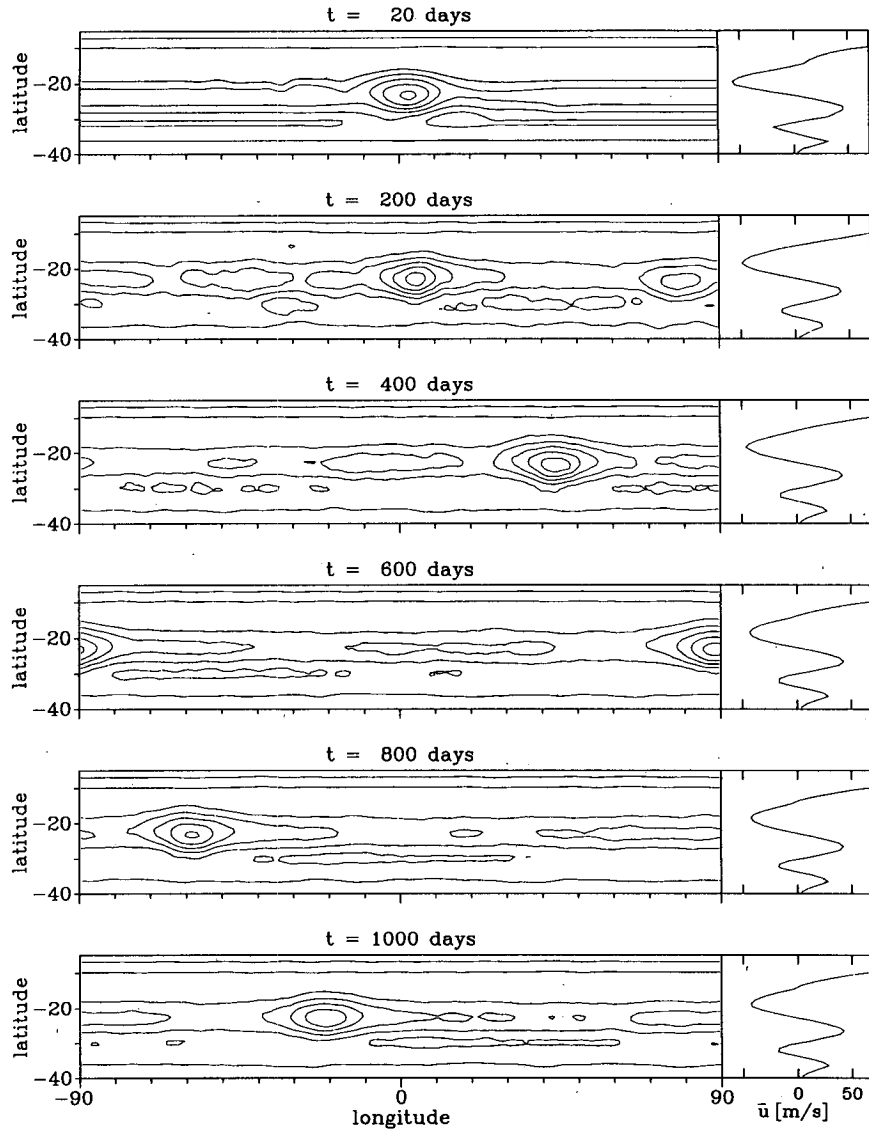
FIG. 9. DI89 run with zonal forcing ($\tau = 400\ d$). Compare with Fig. 8. The vortex drift rate is about 0.22 deg day^{-1}, with a peak wind at $t = 1000$ days of 85 m s^{-1}.

streamlines. For a geostrophic system, contours of $g(h + h_2)$ are coincident with streamlines; i.e., $g(h + h_2)$ is constant along streamlines. The GRS and Oval BC are close enough to geostrophic balance in this context for $g(h + h_2)$ to be quasi-constant on a streamline, as can be seen in Fig. 2. Thus, a Lagrangian $(\zeta + f)$ profile is equal to a quasi-constant that depends on the streamline, $qg(h + h_2)$, plus a term involving the bottom topography, $-qgh_2$ (the constant $-q$ is positive in the Southern Hemisphere). We therefore expect the $(\zeta + f)$ profiles determined for the model vortices to mimic the gh_2 profiles in Fig. 6a, with allowance made for the change in the gh_2 variable when moving from the vortex reference frame to the System III reference frame.

We apply the same algorithm developed for the GRS velocity data in Dowling and Ingersoll (1988) to the model data. Streamlines are computed by first calculating a least-squares fit to the velocity data that fall inside a 3° by 3° averaging box, and then advecting the center of this averaging box accordingly. A typical profile of potential vorticity q, along a streamline, versus latitude is shown in Fig. 14. This profile comes from the largest closed streamline found for the DI89 vortex in Fig. 9, at $t = 1000$ days. The two solid curves are the q values from the east and west parts of the streamline. The noise in q comes from the ζ field which, because we are running the finite difference scheme without an explicit viscosity term, tends to be noisy at the grid scale. The dashed line in Fig. 14 shows the
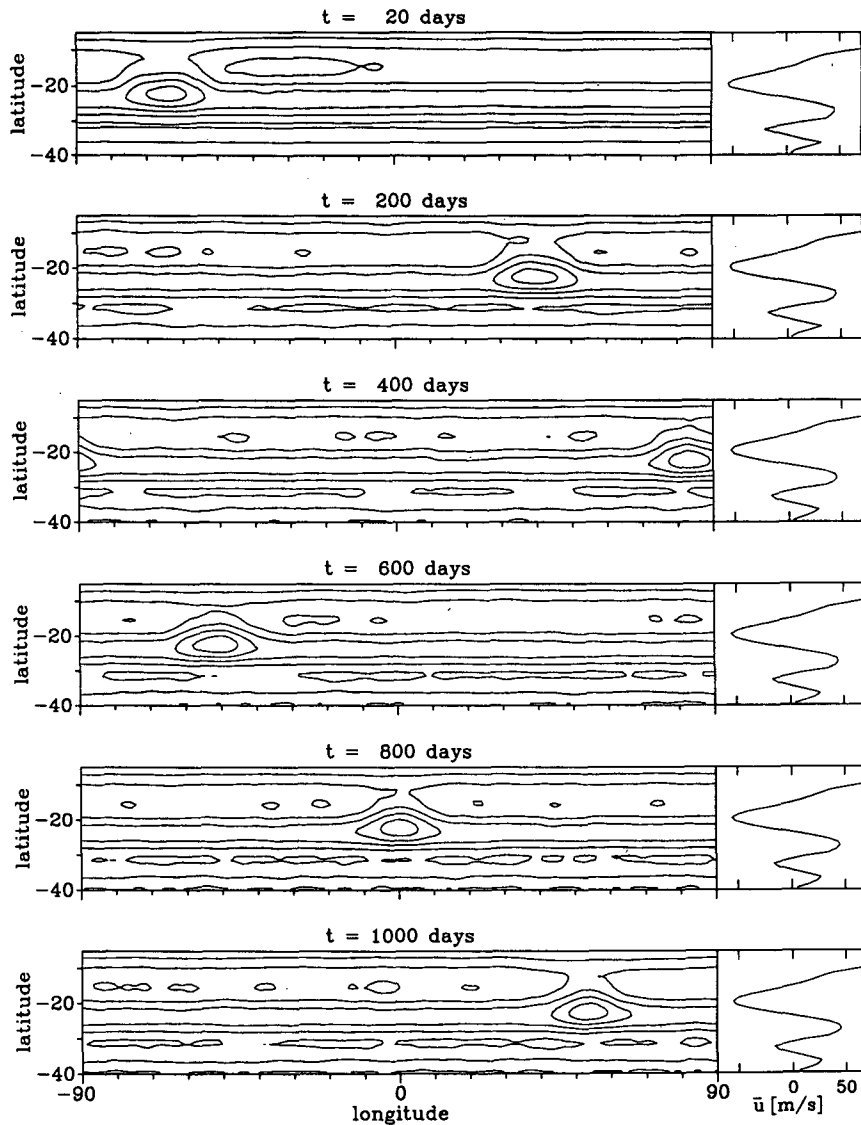
FIG. 10. IC81 run without zonal forcing ($\tau = \infty$). This run is the same as in Fig. 8 except for the change to the IC81 bottom topography shown in Fig. 6a. The vortex drifts at about -3.25 deg day^{-1}, and the peak wind at $t = 1000$ days is 78 m s^{-1}. The vortex moves quickly enough so that the apparent drift from frame to frame is not the actual drift.

mean $\langle q \rangle = -1.60 \times 10^{-9}$ s m^{-2}. The variation about the mean in terms of a standard deviation is 0.1×10^{-9} s m^{-2}, which is 2.6% of the total range of q for this time frame. If we were to use the wrong vortex drift rate in the analysis, off by say 0.5 deg day^{-1}, and thereby calculate an erroneous streamline, the resulting q profile would be noticeably nonconstant. Since the gh variable is quite smooth, a convenient and accurate way of removing the noise in the ζ variable is to use the relation $(\zeta + f) = qgh$, and replace q by the streamline mean $\langle q \rangle$. The $(\zeta + f)$ profiles computed for the model vortices will be presented in this manner.

The results of the Lagrangian vorticity analysis on the model vortices are shown in Fig. 15. In panel (a) we show the DI89 case. The dashed curve is the Coriolis parameter f. The solid curve is from the largest closed streamline, which is analogous to the GRS streamline d in Fig. 13. Notice that the contributions from the left and right halves of the vortex are virtually indistinguishable. The dotted curves are from streamlines analogous to the GRS streamlines f and h in Fig. 13. To the extent that the flow is geostrophic, as discussed above, each of these $(\zeta + f)$ profiles mimics a portion of the DI89 gh_2 profile in Fig. 6a (with a negligible
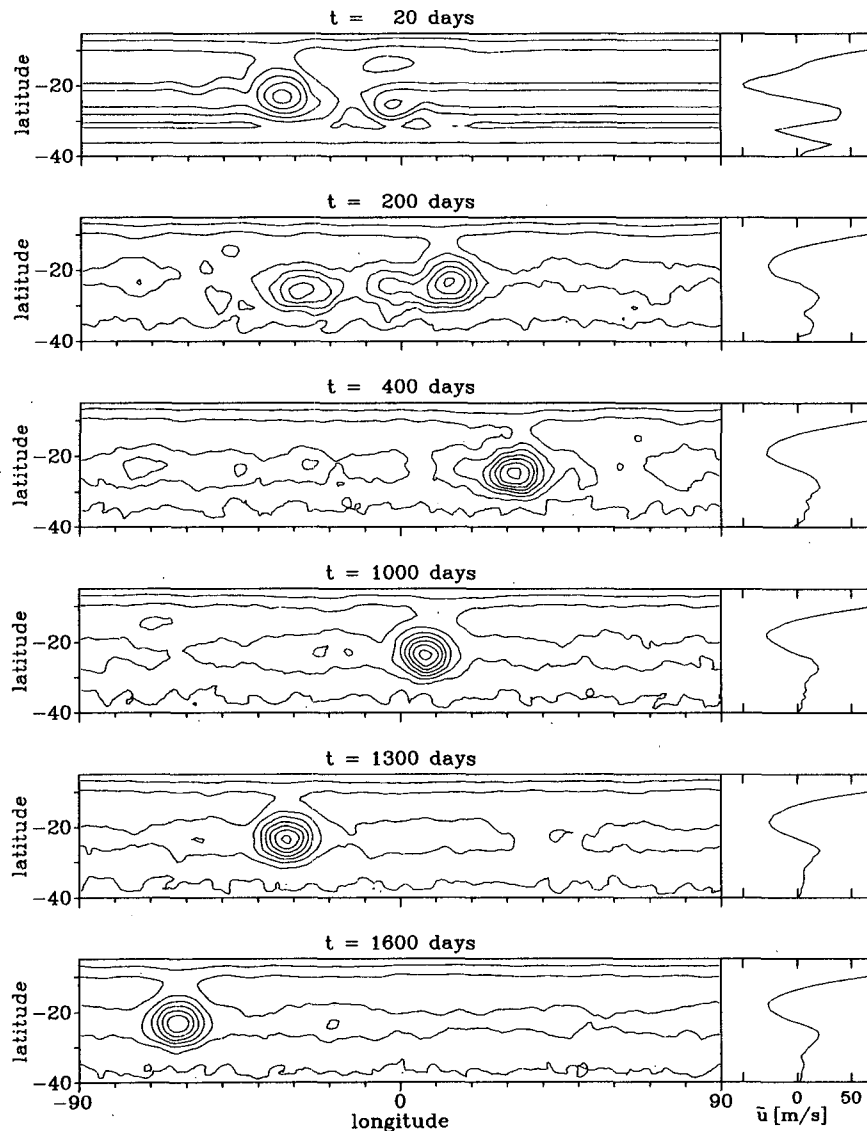
FIG. 11. WY84 run with zonal forcing ($\tau = 400\ d$). This run is the same as in Fig. 9 except for the change to the WY84 bottom topography shown in Fig. 6a. The vortex drifts at about -1.88 deg day^{-1}, and the peak wind at $t = 1600$ days is 105 m s^{-1}. The vortex moves quickly enough so that the apparent drift from frame to frame is not the actual drift.

reference frame correction). The $(\zeta + f)$ profiles are discontinuous even though gh_2 is continuous—a result of the different constants for each streamline. The agreement between the DI89 model and the GRS data is quite good.

The $(\zeta + f)$ profiles from the IC81, WY84, and M88 runs are given in Fig. 15b–d. Each $(\zeta + f)$ profile, taken in the reference frame of the vortex, should be compared with the observations of Fig. 13. This is the crucial test. A side issue is how well the $(\zeta + f)$ profiles mimic the bottom topographies of Fig. 6a. For these models, the vortex drift rates relative to System III are

large enough that care must be taken when comparing Fig. 15 to Fig. 6a. Equation (6) determines how gh_2 transforms under a change of reference frame. The effect is most clearly seen with the WY84 case, where the bottom topography is flat in the System III frame (Fig. 6a), and takes on a slope in the (westward-drifting) vortex frame (Fig. 15c). As can be seen in Fig. 15c, the WY84 vortex "feels" a bottom topography which is higher on the equatorward side and lower on the poleward side. The IC81 and M88 vortices examined here drift westward at a rate similar to the WY84 vortex, and comparison of the Lagrangian $(\zeta + f)$ pro-
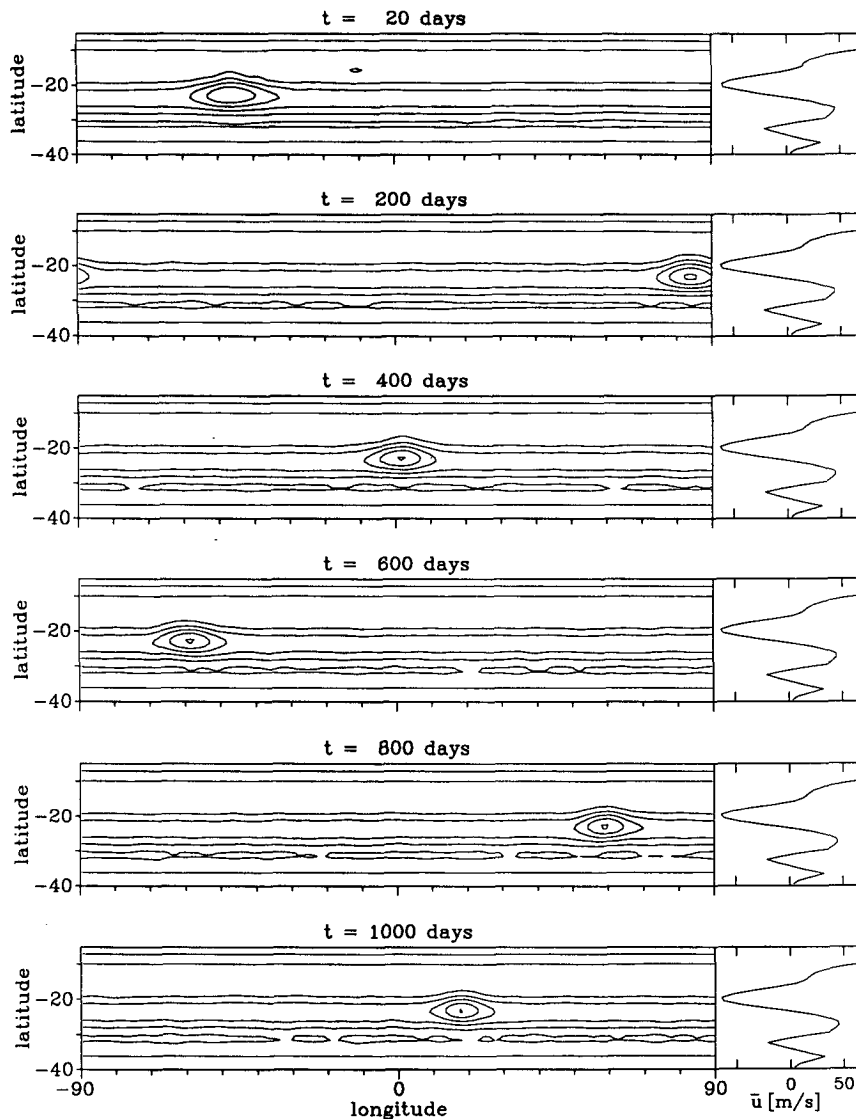
FIG. 12. M88 run without zonal forcing ($\tau = \infty$). This run is the same as in Figs. 8 and 10 except for the change to the M88 bottom topography shown in Fig. 6a. The vortex drifts at about -2.00 deg day^{-1}, and the peak wind at $t = 1000$ days is 123 m s^{-1}. The vortex moves quickly enough so that the apparent drift from frame to frame is not the actual drift.

files in Fig. 15 to the bottom topographies in Fig. 6a requires removing a similar slope. Having taken the reference frame change into account, Figs. 6a and 15 demonstrate that the Lagrangian ($\zeta + f$) profiles of a vortex yield a useful qualitative picture of the bottom topography over which the vortex is traveling.

We conclude from many comparisons of ($\zeta + f$) profiles that only the present DI89 model is in agreement with the observations for the GRS, which is not surprising since the DI89 model is derived from the data. The significance of the agreement is that Lagrangian ($\zeta + f$) profiles are a meaningful test of models,

and other models of the GRS not examined here must pass the same test.

The drift rate of a vortex is found to depend sensitively on the bottom topography, as can be seen by comparing the model runs in Figs. 8–12. In addition, we find (not shown) that model White Oval vortices with the DI89 bottom topography drift eastward at a speed of a few meters per second, which is the correct sign and magnitude for the White Ovals, whereas the same vortices run over a flat bottom (the WY84 model) tend to drift westward. A detailed analysis of SW vortex drift rates, which includes the effects of variable bottom
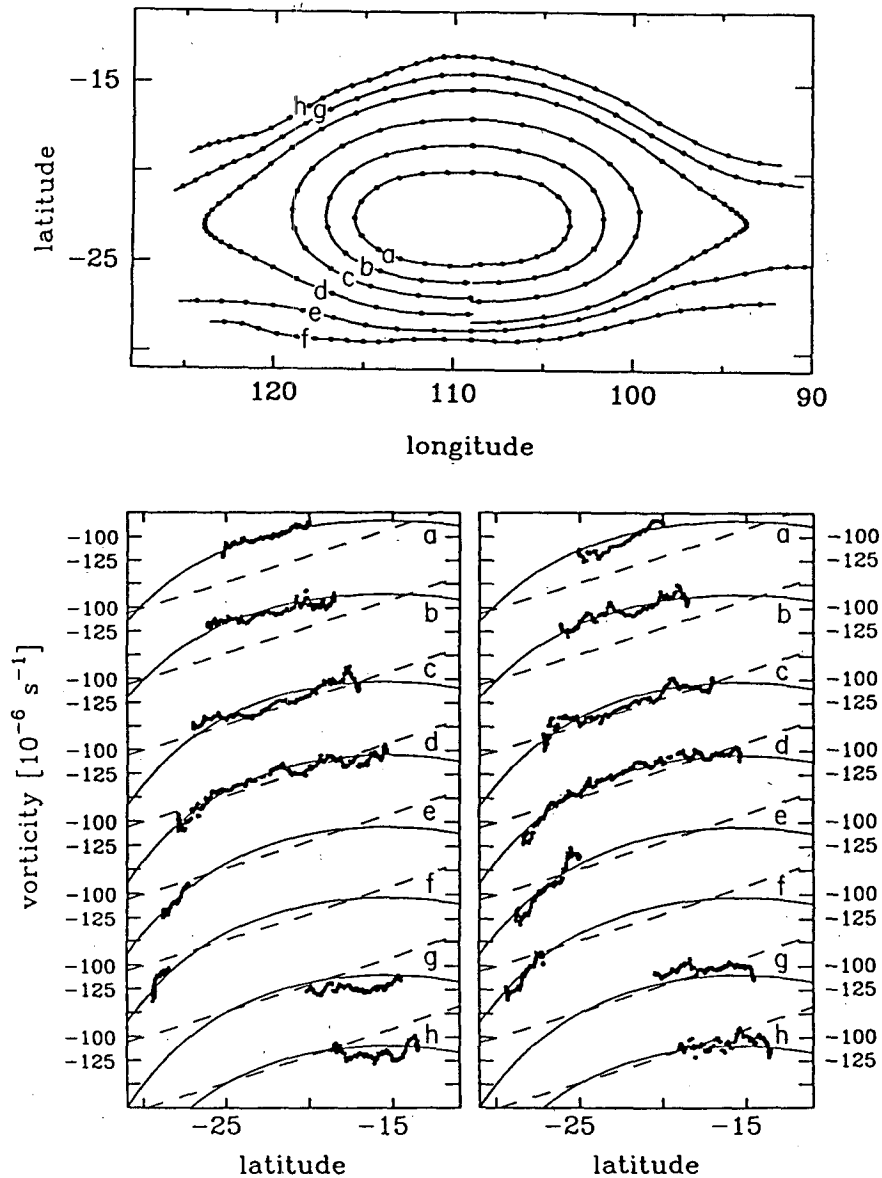
FIG. 13. Lagrangian vorticity analysis results for the GRS from Dowling and Ingersoll (1988). The top panel shows the selected GRS streamlines used in the analysis, labeled a–h. The dots indicate intervals of 10 hours. The bottom panels show absolute vorticity ($\zeta + f$), along streamlines, versus latitude λ. The left and right panels correspond to the streamline segments left (west) and right (east) of 109° longitude, respectively. For each streamline there are three pairs of curves, and these curves are offset from the next by 75×10^{-6} s^{-1} in the ordinate. The heavy dots are the computed ($\zeta + f$). The dashed curves are f. The solid curves are a quadratic least-squares fit to the data. These ($\zeta + f$) profiles are to be compared with those from the same analysis applied to the numerical vortices studied in this section.

topography, is needed, but this has not been attempted in the present paper.

In the section 5b we briefly review proposed mechanisms for the maintenance against dissipation of Jovian vorticies, and examine the longevity and genesis of a DI89 model vortex.

b. Longevity and genesis

The models of Figs. 8–12 have much in common, yet they separate into two classes. In the first class are those for which the basic shear flow is stable. The IC81 and M88 models (Figs. 10 and 12) are in this category.
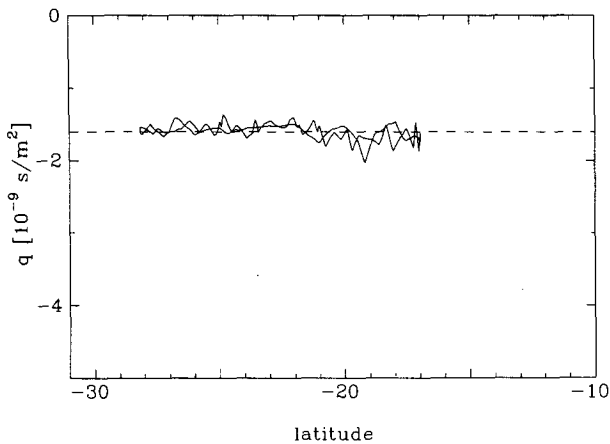
FIG. 14. Typical profile of potential vorticity q, along a streamline, versus latitude λ. This profile comes from the largest closed streamline computed for the DI89 vortex in Fig. 9, at $t = 1000$ days. The two solid curves are the q values from the east and west parts of the streamline. The dashed line shows the mean $\langle q \rangle = -1.60 \times 10^{-9}$ s m^{-2}. The variation about the mean in terms of a standard deviation is 0.1×10^{-9} s m^{-2}, which is 2.6% of the total range of q for this time frame.

Stability is indicated by a lack of significant extrema in the far-field potential vorticity profiles (Fig. 6b), and confirmed by numerical simulations. Since the initial far-field zonal velocity is the same in all models, and is based on observations (Limaye 1986), the difference in far-field potential vorticity from one model to the next arises from the different bottom topographies gh_2, or equivalently, the different deep motions assumed in each model. In the IC81 and M88 models, both the vortices and the shear flows persist indefinitely when introduced as initial conditions in an inviscid calculation (Figs. 10 and 12). We have also run these cases with the forcing/drag term (8), and find that the IC81 and M88 vortices decay slowly with time scale τ (400 days in the cases studied). Both Ingersoll and Cuong (1981) and Marcus (1988) studied the growth of vortices by mergers, when two or more vortices were introduced in the initial conditions. Ingersoll and Cuong proposed that large vortices are maintained against dissipation by absorbing smaller vortices, which they suggested are produced by convection. Mergers are common on Jupiter, and were studied by Mac Low and Ingersoll (1986).

In the other class of models are those for which the basic shear flow is unstable. Again, bottom topography accounts for the difference. According to Fig. 6b, the WY84 model initialized with the Limaye (1986) u_J profile has the most pronounced extrema of $\bar{q}$. The DI89 model also has such extrema. In these models, the zonal shear flow does not persist in an inviscid simulation. Rather, the shear tends to weaken at the expense of small vortices, which are ultimately absorbed by the large vortex. The end result in an inviscid

run is a large vortex that resides indefinitely in a weaker, stabilized shear flow. Figures 9 and 11 show the DI89 and WY84 models with the forcing/drag term (8) included. In contrast to the IC81 and M88 models, the large vortices do not decay in the presence of dissipation. Instead, they maintain themselves against dissipation by absorbing the smaller vortices, which arise spontaneously in the unstable shear flow, and the system achieves a dynamic equilibrium. Thus, we see that merging is common to all the models. The main difference is whether the smaller vortices are introduced to the system or whether they arise spontaneously from the unstable shear flow.

But the question remains, What is happening on Jupiter? Since the present DI89 model uses bottom topography derived from observations, it has special significance. We can ask whether the shear flow produces small vortices, whether these merge spontaneously to form a single large vortex, and whether the vortex persists indefinitely in the presence of dissipation. We cannot rule out additional, unmodeled energy sources such as convection (Ingersoll and Cuong 1981) or diabatic forcing (Read and Hide 1983, 1984; Read 1985, 1986), but we can study longevity and genesis in the context of the reduced-gravity SW model.

In Fig. 16 we show the DI89 run of Fig. 9 extended through ten years. The system is in equilibrium, with the zonal forcing/drag term (8) maintaining the zonal jets in an unstable state. The jets produce small eddies that are absorbed by the large vortex. This process is inherently time dependent, and in many ways resembles the complicated time-dependent interactions observed in Jupiter's atmosphere.

In Fig. 7 we show the results of a vortex genesis experiment. The initial state is constructed by adding a small sinusoidal perturbation of ten wavelengths over the longitudes $-90°$ to $90°$, in a $\text{sech}^2(\phi/90°)$ $\times \sin^{1/2}(-\pi(\lambda + 5°)/35°)$ envelope, to the free-surface height $g(h + h_2)$ calculated from the cloud-top zonal wind profile (Fig. 4), followed by geostrophic initialization of the velocity field. This envelope brings the perturbation of the northward velocity v to zero at the northern and southern boundaries ($\lambda = -5°, -40°$), and adds a slight height difference in longitude to the initial ten waves. The parameters q_0 and τ are as in Fig. 9. The peak initial perturbation velocity is 1.6 m s^{-1}, compared to the 54 m s^{-1} peak initial zonal wind. By $t = 100$ days, the disturbance is noticeable in the $g(h + h_2)$ field. By $t = 300$ days, the initial perturbation has started an instability in the GRS shear flow, which by $t = 500$ days has resolved into three large, distinct vortices. By $t = 750$ days, two of these vortices have merged, and by $t = 1600$ days, only one large vortex remains. This vortex is run through $t = 2000$ days. Notice that even though the initial conditions are vastly different between the run shown here and the run shown in Fig. 16, the final forms are quite similar. We
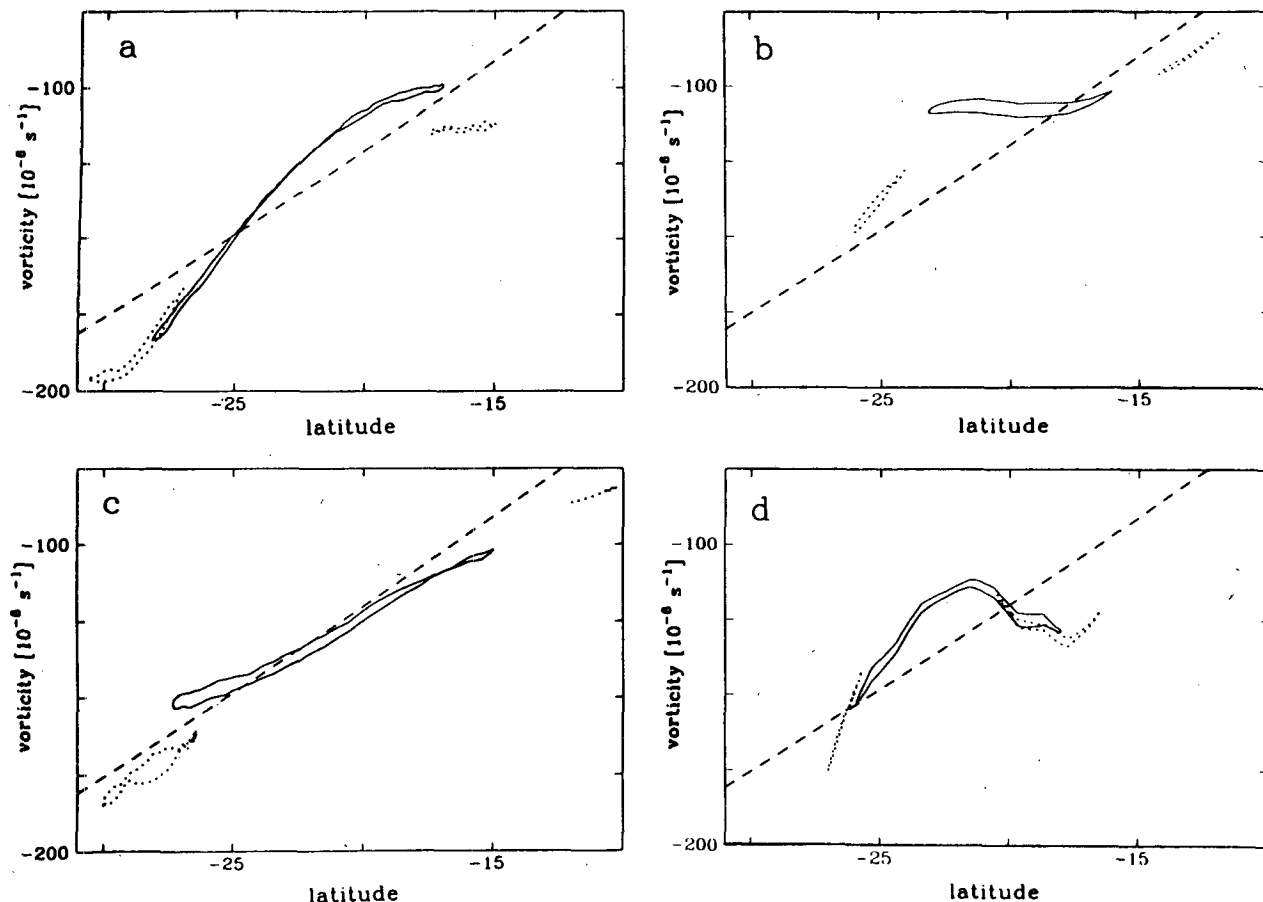
FIG. 15. Absolute vorticity ($\zeta + f$) along streamlines, versus latitude λ for the different numerical models. (a) The DI89 run (Fig. 9) for $t = 1000$ days. The dashed curve is the Coriolis parameter f. The solid curve is from the largest closed streamline, which is analogous to the GRS streamline d in Fig. 13. The dotted curves are from streamlines analogous to the GRS streamlines f and h in Fig. 13. (b) The IC81 run (Fig. 10) for $t = 1000$ days. (c) The WY84 run (Fig. 11) for $t = 1600$ days. (d) The M88 run (Fig. 12) for $t = 1000$ days.

also get the formation of a single large vortex in the shear zone of the GRS if we do not force the zonal flow ($\tau = \infty$), or if we use random noise instead of a sinusoidal perturbation to trigger the instability.

We have demonstrated in this subsection that the existence of a single, large GRS-like vortex on Jupiter follows naturally from the observed cloud-top winds and derived deep atmospheric motions. If the cloud-top winds are kept in an unstable state, the large vortex can be maintained against dissipation indefinitely. This scenario applies to the DI89 and WY84 models, and should be true in general for any other model with an unstable upper-layer zonal velocity profile.

6. Conclusions

We have modeled Jupiter's Great Red Spot (GRS) and deep atmosphere as a shallow water (SW) system. We assume that the Jovian vortices and time-dependent dynamics are confined to a thin upper weather layer, which overlies a deep layer in which the motions are zonal and steady. The dynamical effects of the deep-layer zonal motions on the upper layer are represented, in the reduced-gravity system, by meridionally varying solid bottom topography underneath the upper layer. Most current models of the GRS prescribe this bottom topography, based on assumptions about the deep atmosphere. In this work, we *derive* the bottom topography from the high resolution cloud-top velocity data for the GRS and White Oval BC, up to a single free parameter that depends on the unknown radius of deformation. In the process we calculate the Bernoulli streamfunction B, and determine the potential vorticity q as a function of B.

Our results show that there is differential fluid motion in the deep atmosphere below the vortices. In this sense the models of Williams and Yamagata (1984) and Williams and Wilson (1988), which prescribe flat bottom topography, and hence deep-layer zonal velocity $u_2 = 0$, do not accurately describe Jupiter. The
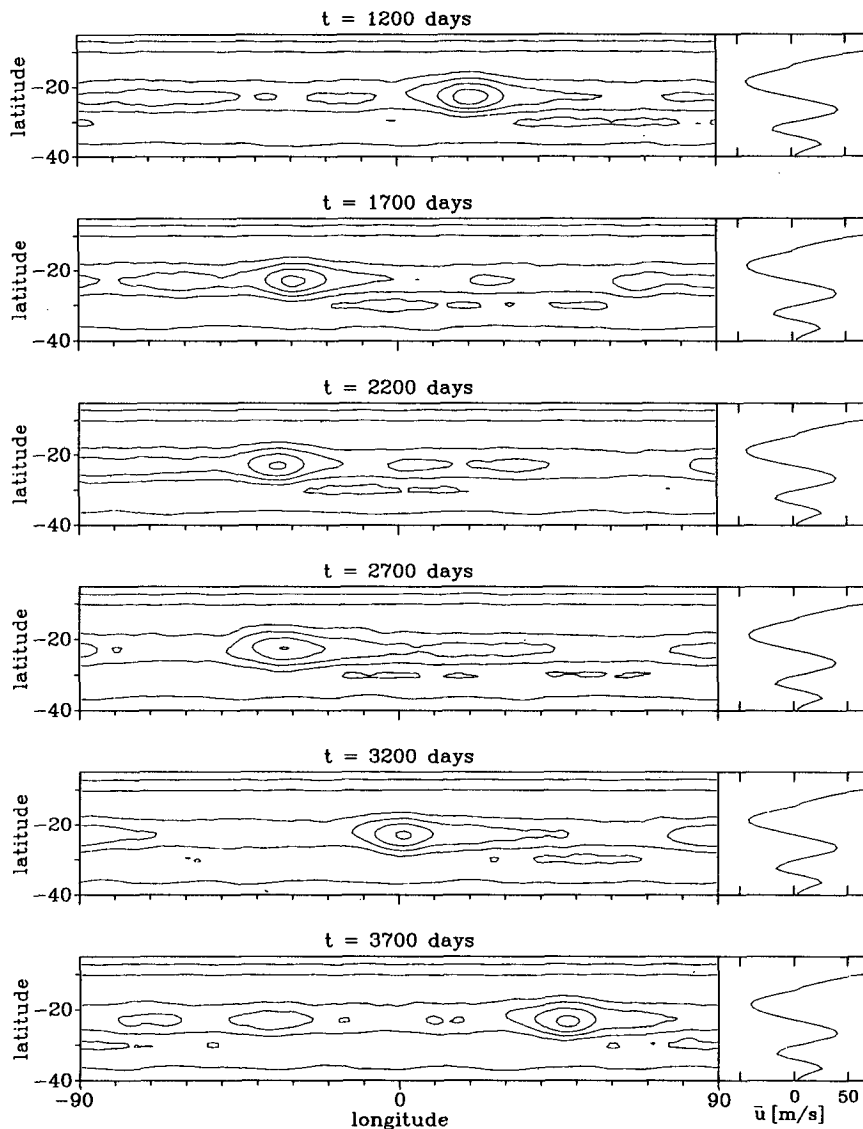
FIG. 16. Longevity experiment. This is the DI89 run of Fig. 9 ($\tau = 400\ d$) extended through ten years. The forcing of the unstable velocity profile continuously produces small vortices that are absorbed by the large vortex, thus maintaining it.

derived deep winds do not correspond exactly with the zonally averaged cloud-top winds. In this sense the model of Ingersoll and Cuong (1981), which prescribes the deep winds to be equivalent to the far-field winds in the upper layer, also does not accurately describe Jupiter. Nor does the model of Marcus (1988), which prescribes uniform far-field potential vorticity, since the derived far-field potential vorticity profile versus latitude contains several extrema.

Since we determine the B field and the functions $q(B)$ for the GRS and Oval BC, we are able to examine the potential vorticity fields associated with these vortices. Both vortices represent minimum $|q|$ anomalies,

and both show q to be relatively uniform inside their closed-streamline regions. The latter observation is consistent with the work of Rhines and Young (1982) on potential vorticity homogenization inside closed-streamline regions.

The filamentary region to the northwest of the GRS has yet to be modeled successfully. We expect that the deep motions must be accurately represented in order to model such a feature. Convective activity may also play an important role in filamentary regions. Convection, were it possible in a SW model, might correspond to negative upper-layer thickness. Our results show that the upper layer is thinnest in the latitude
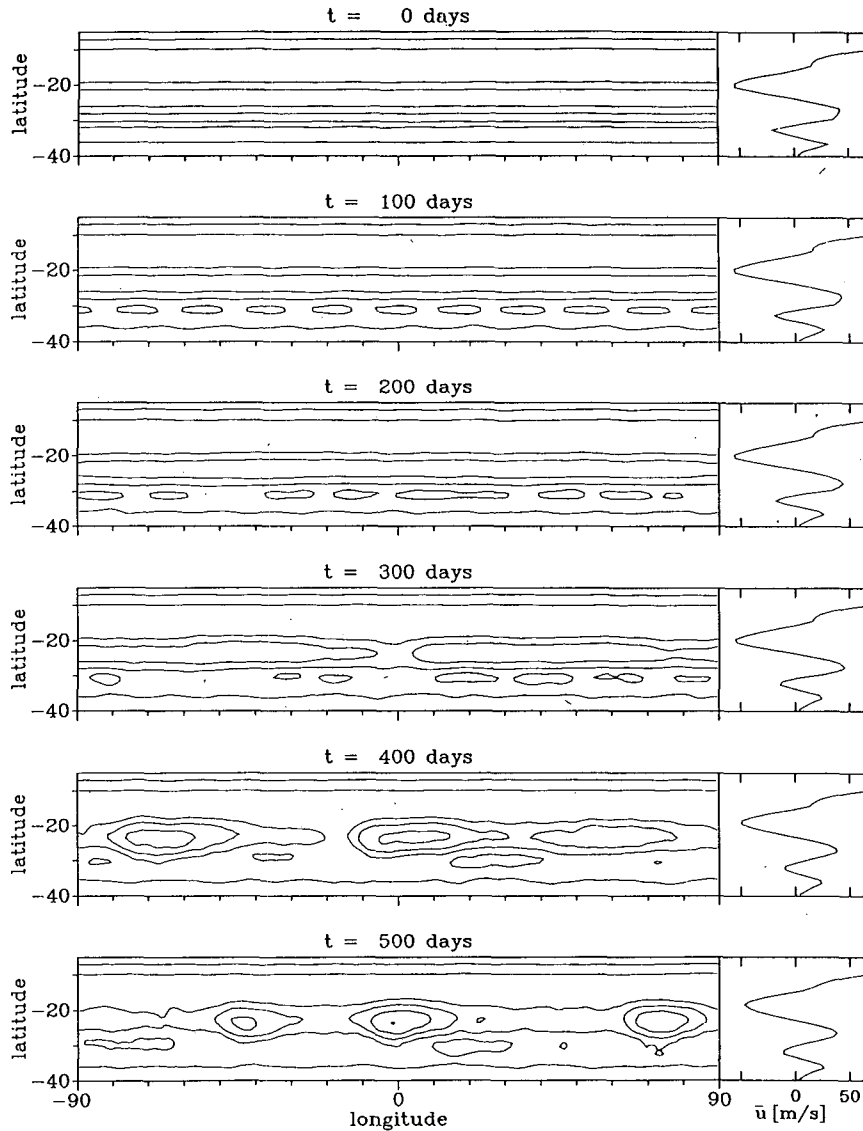
FIG. 17. Genesis experiment. The initial state is constructed by adding a small sinusoidal perturbation of ten wavelengths, in a $\mathrm{sech}^2(\phi/90°)\,\sin^{1/2}(-\pi(\lambda + 5°)/35°)$ envelope, to the free-surface height $g(h + h_2)$ calculated from the cloud-top zonal wind profile (Fig. 4). This envelope brings the perturbation of the northward velocity v to zero at the northern and southern boundaries ($\lambda = -5°, -40°$), and adds a slight longitudinal height difference to the initial ten waves. The specified parameter q_0 is -1.40×10^{-9} s m^{-2} for the GRS. The zonal wind is forced with $\tau = 400\ d$. The peak initial perturbation velocity is 1.6 m s^{-1}, compared to the 54 m s^{-1} peak initial zonal wind. By $t = 500$ days, there are three large, distinct vortices in the GRS's shear flow. By $t = 750$ days, two of these vortices have merged, and by $t = 1600$ days, only one large vortex remains. This vortex is run through $t = 2000$ days. Even though the initial conditions are vastly different for the run shown here and the run shown in Fig. 16, the final forms are quite similar.

range of the GRS's filamentary region, and that the cloud-top winds decay rapidly with depth there.

Using numerical simulations, we have studied the time-dependent behavior of the shallow water analog of Jupiter's atmosphere. We initialize the numerical model with the observed zonally averaged cloud-top velocity profile. In the first class of numerical experiments, we compare the effects of the derived bottom topography to the bottom topographies prescribed by current models. Each of these models is successful in maintaining a long-lived, isolated vortex, but only the present model, which is based on observations, yields
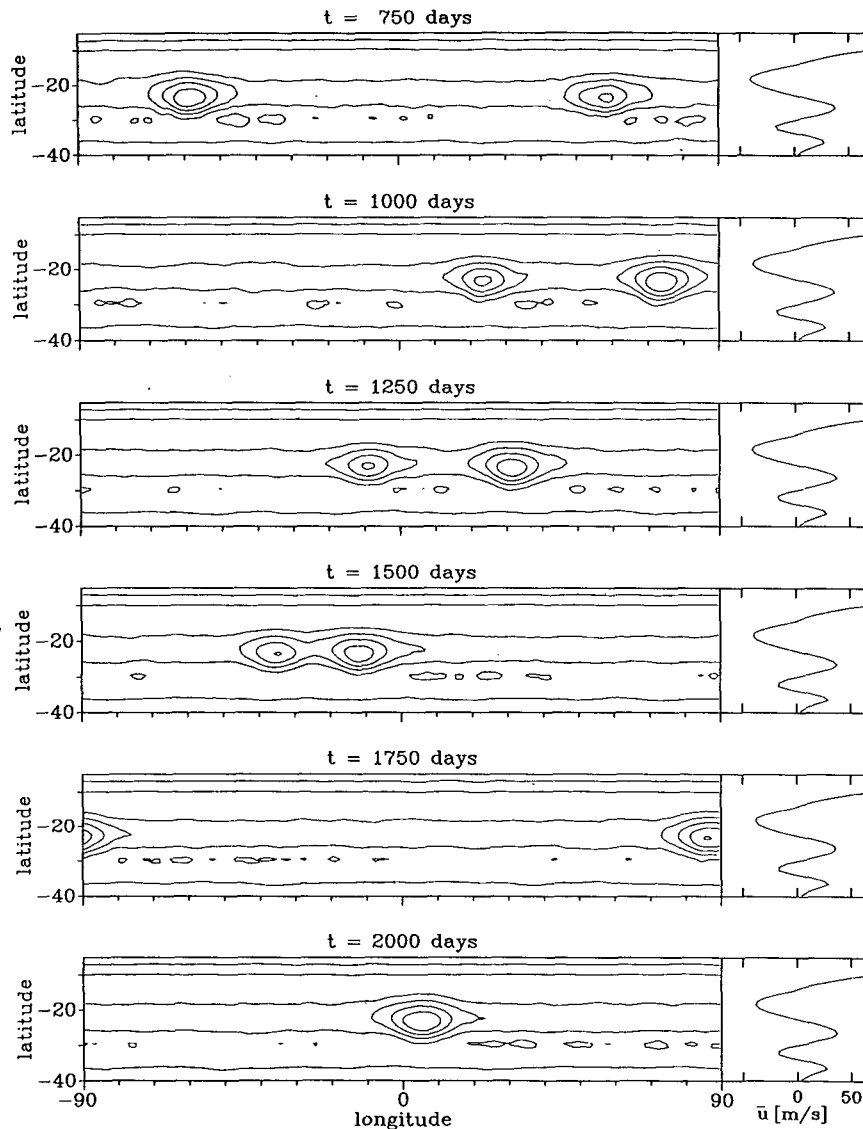
FIG. 17. (*Continued*)

($\zeta + f$) profiles along vortex streamlines that agree with those observed for the GRS by Dowling and Ingersoll (1988).

In the second class of numerical experiments, we study the longevity and genesis of a GRS-like vortex, using the observed cloud-top winds and the derived bottom topography. In this simulation small eddies form in the shear zone associated with the GRS. Such instability is consistent with the local extrema observed in the far-field potential vorticity profile for this model. If the upper-layer eastward velocity u is forced towards the observed profile u_J, the instability is maintained and small eddies appear continuously. These eddies coalesce over a time scale of years into a single, large vortex, which resembles the GRS. This large vortex persists indefinitely against dissipation by absorbing the

constant supply of smaller eddies. Williams and Wilson (1988) arrived at the same conclusion for the case of flat bottom topography.

Our work points out the need to find mechanisms that maintain the observed zonally averaged cloud-top velocity profile, and the derived deep motions. Both the DI89 and WY84 models have an unstable upper-layer zonal velocity profile, which is sufficient for the genesis and maintenance against dissipation of vortices in these models. This does not rule out an additional role in Jupiter's atmosphere for eddies produced by convection. Such eddies might be a source of energy to both the unstable zonal flow and the large vortices.

The manner in which these large vortices maintain themselves against inviscid destructive processes is not directly addressed in this paper. For the flat-bottom

case, Williams and Wilson (1988) studied the balances among the translation, twisting, steepening, dispersion, and advection processes. Ingersoll and Cuong (1981) and Marcus (1988) focused on radiation of energy by Rossby waves, and chose bottom topographies that did not allow such radiation. The present work indicates that the above models with prescribed bottom topography do not accurately describe Jupiter. Clearly, it would be interesting to extend the work of Williams and Wilson (1988) to include variable bottom topography, and to relax the restrictions in Ingersoll and Cuong (1981) and Marcus (1988) to include Rossby wave radiation.

We have emphasized a reduced-gravity interpretation of the data, with a single layer and variable bottom topography, because such a model contains the minimum amount of complexity to explain the observations, and because most current models of the GRS are cast in terms of such a model. In this model, the observed variation of $(\zeta + f)$ along streamlines, i.e., the observed vortex-tube stretching, is accounted for by deep zonal motions underneath the vortices. Other sources of vortex-tube stretching are possible. If the Jovian troposphere and its vortices are modeled with two or more layers instead of just one weather layer, it is conceivable that $(\zeta + f)$ variations may arise due to vortex-tube stretching that occurs locally near the cloud-top level, instead of being distributed over the entire weather layer. Nevertheless, any such alternate model of the GRS must be able to reproduce the observed Lagrangian $(\zeta + f)$ profiles, and hence account for the vortex-tube stretching occurring in the cloud-top flow. The DI89 model, since it is based on observations, is the first to pass this test.

REFERENCES

Achterberg, R. K., and A. P. Ingersoll, 1989: A normal mode approach to Jovian atmospheric dynamics. *J. Atmos. Sci.*, 46, 2448–2462.

Allison, M. D., and P. J. Gierasch, 1982: Jovian atmospheric dynamics: Global-scale motion and shear instability for a thin, nearly adiabatic upper weather layer. *Bull. Amer. Astron. Soc.*, 14, 722.

Arakawa, A., and V. R. Lamb, 1981: A potential enstrophy and energy conserving scheme for the shallow water equations. *Mon. Wea. Rev.*, 109, 18–36.

Dowling, T. E., and A. P. Ingersoll, 1988: Potential vorticity and layer thickness variations in the flow around Jupiter's Great Red Spot and White Oval BC. *J. Atmos. Sci.*, 45, 1380–1396.

Flasar, F. M., 1986: Global dynamics and thermal structure of Jupiter's atmosphere. *Icarus*, 65, 280–303.

——, and P. J. Gierasch, 1986: Mesoscale waves as a probe of Jupiter's deep atmosphere. *J. Atmos. Sci.*, 43, 2683–2707.

——, B. J. Conrath, J. A. Pirraglia, P. C. Clark, R. G. French and P. J. Gierasch, 1981: Thermal structure and dynamics of the Jovian atmosphere. 1. The Great Red Spot. *J. Geophys. Res.*, 86, 8759–8767.

Flierl, G. R., 1984: Rossby wave radiation from a strongly nonlinear warm eddy. *J. Phys. Ocean.*, 14, 47–58.

Gill, A. E., 1982: *Atmosphere–Ocean Dynamics.* Academic Press, p. 120.

Haltiner, G. J., and R. T. Williams, 1980: *Numerical Prediction and Dynamic Meteorology.* Wiley and Sons, pp. 134, 153–157.

Ingersoll, A. P., 1988: Models of Jovian vortices. *Nature*, 331, 654–655.

——, and P. G. Cuong, 1981: Numerical model of long-lived Jovian vortices. *J. Atmos. Sci.*, 38, 2067–2076.

——, R. F. Beebe, B. J. Conrath and G. E. Hunt, 1984: Structure and dynamics of Saturn's atmosphere. *Saturn.* T. Gehrels and M. S. Matthews, Eds., University of Arizona Press, 195–238.

——, S. A. Collins, G. E. Hunt, J. L. Mitchell, P. Muller, B. A. Smith and R. J. Terrile, 1979: Zonal velocity and texture in the Jovian atmosphere inferred from Voyager images. *Nature*, 280, 773–775.

Limaye, S. S., 1986: Jupiter: New estimates of the mean zonal flow at the cloud level. *Icarus*, 65, 335–352.

Mac Low, M.-M., and A. P. Ingersoll, 1986: Merging of vortices in the atmosphere of Jupiter: An analysis of *Voyager* images. *Icarus*, 65, 353–369.

Marcus, P. S., 1988: A numerical simulation of the Great Red Spot of Jupiter. *Nature*, 331, 693–696.

Mitchell, J. L., R. F. Beebe, A. P. Ingersoll and G. W. Garneau, 1981: Flow fields within Jupiter's Great Red Spot and White Oval BC. *J. Geophys. Res.*, 86, 8751–8757.

Pedlosky, J., 1987. *Geophysical Fluid Dynamics,* Second Edition. Springer-Verlag.

Read, P. L., 1985. Finite-amplitude, neutral baroclinic eddies and mean flows in an internally heated rotating fluid: 1. Numerical simulations and quasi-geostrophic "free modes." *Dyn. Atmos. Oceans,* 9, 135–207.

——, 1986: Stable, baroclinic eddies on Jupiter and Saturn: A laboratory analog and some observational tests. *Icarus,* 65, 304–334.

——, and R. Hide, 1983: Long-lived eddies in the laboratory and in the atmospheres of Jupiter and Saturn. *Nature,* 302, 126–129.

——, and ——, 1984: An isolated baroclinic eddy as a laboratory analogue of the Great Red Spot on Jupiter? *Nature,* 308, 45–49.

Rhines, P. B., and W. R. Young, 1982: Homogenization of potential vorticity in planetary gyres. *J. Fluid Mech.,* 122, 347–367.

Ripa, P., 1983: General stability conditions for zonal flows in a one-layer model on the β-plane or the sphere. *J. Fluid Mech.,* 126, 463–489.

Smith, B. A., L. A. Soderblom, T. V. Johnson, A. P. Ingersoll, S. A. Collins, E. M. Shoemaker, G. E. Hunt, H. Masursky, M. H. Carr, M. E. Davies, A. F. Cook II, J. Boyce, G. E. Danielson, T. Owen, C. Sagan, R. F. Beebe, J. Veverka, R. G. Strom, J. F. McCauley, D. Morrison, G. A. Briggs and V. E. Suomi, 1979a: The Jupiter system through the eyes of *Voyager 1. Science,* 204, 951–972.

——, R. Beebe, J. Boyce, G. Briggs, M. Carr, S. A. Collins, A. F. Cook II, G. E. Danielson, M. E. Davies, G. E. Hunt, A. P. Ingersoll, T. V. Johnson, H. Masursky, J. McCauley, D. Morrison, T. Owen, C. Sagan, E. M. Shoemaker, R. Strom, V. E. Suomi and J. Veverka, 1979b: The Galilean satellites and Jupiter: *Voyager 2* imaging science results. *Science,* 206, 927–950.

Stevenson, D. J., 1982: Interiors of the giant planets. *Annu. Rev. Earth Planet. Sci.,* 10, 257–295.

Williams, G. P., and T. Yamagata, 1984: Geostrophic regimes, intermediate solitary vortices and Jovian eddies. *J. Atmos. Sci.,* 41, 453–478.

——, and R. J. Wilson, 1988: The stability and genesis of Rossby vortices. *J. Atmos. Sci.,* 45, 207–241.